

Physics of Stellar Coronae

Manuel Güdel

Paul Scherrer Institut, Würenlingen and Villigen, CH-5232 Villigen PSI,
Switzerland guedel@astro.phys.ethz.ch

1 Introduction

For the plasma physicist, the solar corona offers an outstanding example of a space plasma, and surely one that deserves a lifetime of study. Not only can we observe the solar corona on scales of a few hundred kilometers and monitor its changes in the course of seconds to minutes, we also have a wide range of detailed diagnostics at our disposal that provide immediate access to the prevalent physical processes.

Yet, solar physics offers a rich field of unsolved plasma-physical problems. How is the coronal plasma continuously heated to $> 10^6$ K? How and where are high-energy particles episodically accelerated? What is the internal dynamics of plasma in magnetic loops? What is the initial trigger of a coronal flare? How does the corona link to the solar wind, and how and where is the latter accelerated? How is plasma transported into the solar corona?

Why, then, study stellar coronae that remain spatially unresolved in X-rays and are only marginally resolved at radio wavelengths, objects that require exposure times of several hours before approximate measurements of the ensemble of plasma structures can be obtained?

There are many reasons. In the context of the *solar-stellar connection*, stellar X-ray astronomy has introduced a range of stellar rotation periods, gravities, masses, and ages into the debate on the magnetic dynamo. Coronal magnetic structures and heating mechanisms may vary together with variations of these parameters. Parameter studies could provide valuable insight for constraining relevant theory. Different topologies and sizes of magnetic field structures lead to different wind mass-loss rates, and this will regulate the stellar spin-down rates differently.

Including stars into the big picture of coronal research has also widened our view of coronal plasma physics. While solar coronal plasma resides typically at $(1 - 5) \times 10^6$ K with temporary excursions to ≈ 20 MK during large flares, much higher temperatures are found on some active stars, with steady plasma temperatures of several tens of MK and flare peaks beyond 100 MK. Energy release in stellar flares involves up to 10^5 times more thermal energy than in solar flares, and pressures that are not encountered in the solar corona.

Table 1. Symbols and units used throughout the text

Symbol, acronym	Explanation
R_* or R	Stellar radius [cm]
R_\odot	Solar radius [7×10^{10} cm]
c	Speed of light [3×10^{10} cm s ⁻¹]
k	Boltzmann constant [1.38×10^{-16} erg cm ³ K ⁻¹]
m_e	Mass of electron [9.1×10^{-28} g]
d	Distance [pc]
p	Pressure [dyne cm ⁻²]
L	Coronal loop semi-length [cm]
T	Coronal electron temperature [K]
T_b	Radio brightness temperature [K]
n, N	non-thermal electron density (N : integrated in energy)
N	Number of flares
n_e	Electron density [cm ⁻³]
n_H	Hydrogen density [cm ⁻³]
B	Magnetic field strength [G]
f	Surface filling factor [%]
Γ	Loop area expansion factor (apex to base)
E	Energy [erg]
L_R	Radio luminosity [erg s ⁻¹ Hz ⁻¹]
L_X	X-ray luminosity [erg s ⁻¹]
L_{bol}	Stellar bolometric luminosity [erg s ⁻¹]
$\Lambda = \Lambda_0 T^\alpha$	Cooling function [erg s ⁻¹ cm ³]
τ	(Decay) time scales, also: optical depth
ν	Radio frequency
ν_p, ω_p	Plasma frequency, angular plasma frequency
ν_c, Ω_c	Gyrofrequency, angular gyrofrequency
κ	Absorption coefficient
γ	Lorentz factor
L_B	Magnetic scale height
HRD	Hertzsprung-Russell Diagram
EM	Emission Measure
Q, DEM	Differential Emission Measure Distribution
EMD	(discretized, binned) Emission Measure Distribution

The present chapter provides a “stellar astronomer’s view” of magnetic coronae. It cannot replace the knowledge of detailed physical processes in the solar corona, nor do we expect to find entirely new physical concepts from the study of stellar coronae without guidance by solar physics. However, as I hope to show in the following sections, stellar astronomy has provided some unexpected and systematic trends that may well help understand systematics of coronal behavior across a large range of stellar parameters. In this sense, the goal of this chapter is to present an overview of the basic, observed stellar-coronal phenomena and their interpretation analogous to solar physics, rather

than the derivation of the basic plasma-physical mechanisms themselves. For a deeper understanding of the latter, I must refer the reader to appropriate textbooks and lectures on solar coronal physics.

2 Stellar coronae - Defining the theme

We consider coronae to be the ensemble of closed magnetic structures above the stellar photosphere and chromosphere together with their plasma content, regardless of whether the latter is the thermal bulk plasma or a non-thermal population of accelerated particles. Although often narrowed down to some specific energy ranges, coronal emission is intrinsically a multi-wavelength phenomenon revealing itself from the meter-wave radio range to gamma rays. The most important wavelength regions from which we have learned *diagnostically* on *stellar* coronae include the radio (decimetric to centimetric) range and the X-ray domain. The former is sensitive to accelerated electrons in magnetic fields, and that has provided the only direct means of imaging stellar coronal structure, through very long baseline interferometry.

The soft X-ray (0.1–10 keV) diagnostic power has been instrumental for our understanding of physical processes in the hot, magnetically trapped coronal plasma, and the recent advent of high-resolution X-ray spectroscopy with the *Chandra* and *XMM-Newton* X-ray observatories is now accessing physical parameters of coronal plasma directly. The adjacent extreme ultraviolet (EUV) range contains diagnostic relevant for the same temperature range as X-rays.

3 The coronal Hertzsprung-Russell diagram

Before discussing specific physical problems in stellar coronal physics, I will briefly review the phenomenology of stellar radio (here: 1–20 GHz) and X-ray emission and summarize stellar classes that are prolific coronal emitters. Fig. 1 presents Hertzsprung-Russell diagrams (HRD) of detected X-ray (left) and radio (right) stars. They show all basic features that we know from an optical HRD. Although the samples used for these figures are in no way “complete” (in volume or brightness), the main sequence is clearly evident, and so is the giant branch. The cool half of the subgiant and giant area is dominated by the X-ray and radio-strong sample of RS CVn and Algol-type close binaries. The top right part of the diagram, comprising cool giants, is almost devoid of X-ray detections, however (although well populated by radio emitters). The so-called corona vs. wind dividing line (dashed in Fig. 1a; after Linsky & Haisch 1979) separates coronal giants and supergiants to its left from stars with massive winds to its right. It is unknown whether the wind giants possess magnetically structured coronae at the base of their winds

– the X-rays may simply be absorbed by the overlying wind material. Additionally, a very prominent population of (presumably) coronal radio and X-ray sources just above the main sequence is made up of various classes of pre-main sequence stars, such as classical and weak-lined T Tauri stars.

Moving toward A-type stars on the HRD, one expects, and finds, a significant drop of coronal emission owing to the absence of magnetic dynamo action in these stars. However, this is also the region of the chemically peculiar Ap/Bp stars that possess strong magnetic fields and many of which are now known to be non-thermal radio sources as well. Finally, the very luminous radio and X-ray emissions from O and B stars are believed to originate in non-magnetic stellar winds - we will not further discuss these stars.

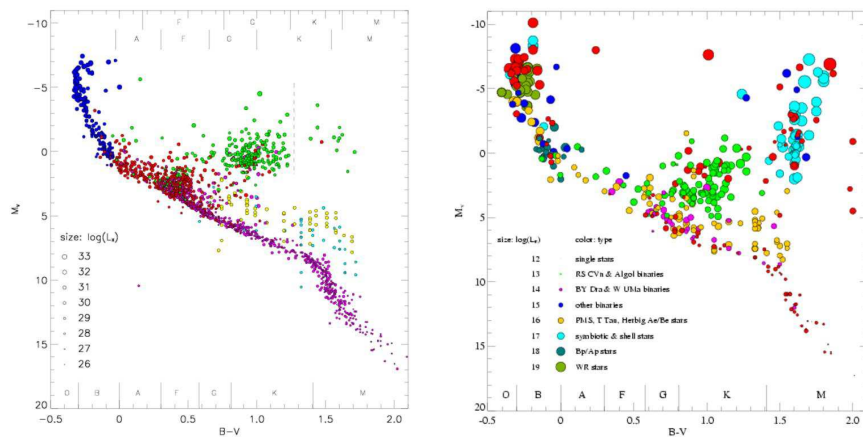


Fig. 1. Left: Hertzsprung-Russell diagram based on about 2000 X-ray detected stars extracted from survey catalogs (see Güdel 2004 for references). The size of the circles characterizes $\log L_X$ as indicated in the panel at lower left. The ranges for the spectral classes are given at the top (upper row for supergiants, lower row for giants), and at the bottom of the figure (for main-sequence stars). – **Right:** Similar, but for 440 radio stars detected between 1–10 GHz (after Güdel 2002).

4 Nonflaring radio emission from stellar coronae

“Quiescent” (non-flaring) radio emission at levels of $10^{12} - 10^{16} \text{ erg s}^{-1} \text{ Hz}^{-1}$ from magnetically active stars was entirely unanticipated but constitutes an important achievement in stellar radio astronomy: There simply is no solar counterpart! Quiescent emission can be defined by the absence of impulsive, rapidly variable flare-like events. Common characteristics of quiescent emission are (i) slow variations on time scales of hours and days, (ii) broad-band

radio spectra, (iii) brightness temperatures in excess of coronal temperatures measured in X-rays, and usually (iv) low polarization degrees.

4.1 Bremsstrahlung

The Sun emits steady, full-disk, optically thick thermal radio emission at chromospheric and transition region levels of a few 10^4 K. However, such emission cannot be detected with present-day facilities, except for radiation from the very nearest stars, or giants subtending a large solid angle. Using the Rayleigh-Jeans approximation for the flux density S

$$S = \frac{2kT\tau\nu^2}{c^2} \frac{\pi R^2}{d^2} \approx 0.049 \left(\frac{T}{10^6 \text{ K}} \right) \left(\frac{\nu}{1 \text{ GHz}} \right)^2 \left(\frac{R}{R_\odot} \right)^2 \left(\frac{1 \text{ pc}}{d} \right)^2 \tau \text{ mJy} \quad (1)$$

(R = source radius, T = electron temperature, d = stellar distance, k = Boltzmann constant, ν = observing frequency, τ = optical depth), we find for optically thick chromospheric emission (with $\tau = 1$, $T = 1.5 \times 10^4$ K, $\nu = 8.4$ GHz)

$$S \approx \frac{0.05}{d_{\text{pc}}^2} \left(\frac{R}{R_\odot} \right)^2 \text{ mJy}. \quad (2)$$

Optically thin free-free emission from the hot, X-ray emitting plasma in coronal loops can be estimated as follows: The radio optical depth is

$$\tau = \int \kappa dl \approx \frac{0.16}{\nu^2 T^{3/2}} \int n_e^2 dl \quad (3)$$

and the X-ray volume emission measure EM, using a filling factor f in the approximation of a small coronal height,

$$\text{EM}_X = 2R^2 \pi f \int n_e^2 dl. \quad (4)$$

(the factor of two accounts for the visible and invisible hemispheres, assuming that the EM is uniformly distributed). For plasma between 1–20 MK, the EM can be estimated from the X-ray luminosity L_X with a conversion factor $\Lambda(T)$ (Mewe et al. 1985, Λ larger for lower T)

$$L_X = \Lambda(T) \text{EM}_X \approx (1.5 - 6) \times 10^{-23} \text{EM}_X \quad [\text{erg s}^{-1}] \quad (5)$$

Thus, we find (using $T_{\text{MK}} = T/[10^6 \text{ K}]$)

$$S = 2.6 \times 10^{-52} \frac{L_X}{\Lambda(T) T_{\text{MK}}^{1/2} f d_{\text{pc}}^2} \text{ mJy} \approx (4 - 17) \times 10^{-30} \frac{L_X}{T_{\text{MK}}^{1/2} f d_{\text{pc}}^2} \text{ mJy}. \quad (6)$$

Coronal bremsstrahlung contributions are presently out of reach for almost all stars.

4.2 Gyroresonance emission

Because active stars show high coronal temperatures and large magnetic filling factors that prevent magnetic fields from strongly diverging with increasing height, the radio optical depth can become significant at coronal levels owing to gyroresonance absorption. This type of emission is observed above solar sunspots. The optical depth for the s th harmonic is (after White et al. 1994)

$$\begin{aligned} \tau(s, \nu) &= \frac{\pi^3}{4} \frac{\nu_p L_B}{\nu_c} \frac{s^2 (2s-2)!}{2^{2s-2} s! [(s-1)!]^2} \left(\frac{s^2}{2\mu} \right)^{s-1} \\ &= 1.45 \frac{L_B}{R_*} \frac{R_*}{R_\odot} \frac{n_e}{\nu_{\text{GHz}}} (1.3 \times 10^{-4}, 4.1 \times 10^{-6}, 1.8 \times 10^{-7}) \left(\frac{T}{20 \text{ MK}} \right)^{s-1} \quad (7) \end{aligned}$$

where the three coefficients in the parenthesis are for the harmonics $s = 3, 4$, and 5 , respectively, of the gyrofrequency, ν_{GHz} is the observing frequency in GHz, n_e is the electron density of the emitting hot plasma at temperature T , and $\mu = m_e c^2 / kT$. The magnetic scale height, L_B , is not precisely known but will be assumed to be $0.3R_*$ (see arguments in White et al. 1994). Using typical X-ray derived temperatures ($[1-3] \times 10^7$) and X-ray emission measures $\text{EM} = n_e^2 V$ (to estimate electron densities in the emitting volume), one finds that τ invariably reaches unity at $s = 3, 4$, or 5 for an observing frequency of 15 GHz while $\tau < 1$ for larger s . The highest harmonic that is still optically thick is relevant.

The measured flux from the optically thick layer is then again given by (1). Observations have shown the following:

- The observed fluxes at 15 GHz from M dwarfs are not compatible with the above prediction if the emitting layer of hot plasma covers the entire stellar surface. The observed flux is typically much smaller. The microwave spectra are falling, not compatible with optically thick radiation (White et al. 1994 - see Fig. 2).
- There are exceptions in which a rising spectrum from 5 to 15 GHz (Fig. 2) could be explained by gyroresonance emission, while the lower-frequency spectrum cannot (Güdel & Benz 1989). The same stars may show this feature only temporarily.

These results imply that the hot plasma in general is not coincident with the strong-magnetic field regions in the corona. It must reside in lower- B regions in between or above the cooler regions, possibly implying rather extended coronal structures seen in X-rays. This plasma could be induced by flares in which magnetic loops reconnect to larger structures in which the low-density gas will not produce appreciable gyroresonance emission (White et al. 1994). The cooler plasma also usually observed in active stars might be trapped in the strong fields but its gyroresonance emission is also negligible.

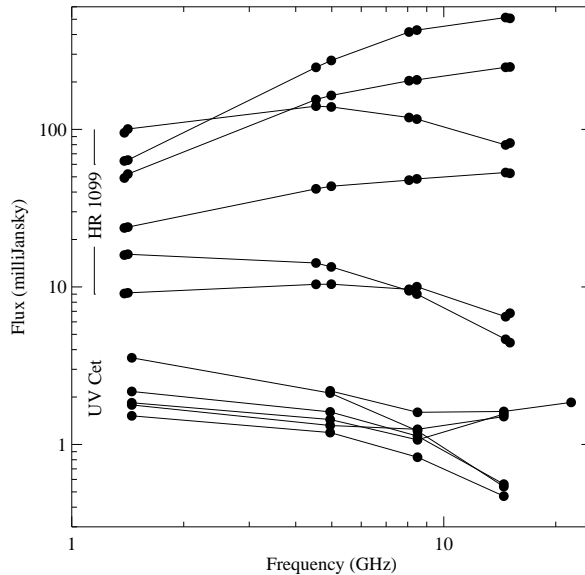


Fig. 2. Radio spectra of the RS CVn binary HR 1099 (upper set) and of the dMe dwarf UV Cet (lower set) at different flux levels. The gently bent spectra are indicative of gyrosynchrotron emission, and the high-frequency part of U-shaped spectra for UV Cet has been interpreted as a gyroresonance component (HR 1099 spectra: courtesy of S. M. White).

Lower-frequency radio emission cannot be due to gyroresonance absorption: The radius of the optically thick layer would still at $s = 3 - 5$, but it would then be located at $> 3R_*$ (for dMe stars). If we extrapolate the the corresponding magnetic fields of more than 100 G down to photospheric levels, we would find photospheric field strengths much in excess of those observed (Gary & Linsky 1981).

4.3 Gyrosynchrotron emission

We could, however, allow for much higher T_{eff} . The optically thick layer would in that case shift to harmonics above 10, the range of gyrosynchrotron radiation. The optically thick source sizes are then more reasonable for M dwarfs, with $R \approx R_*$ (Linsky & Gary 1983), and the optically thin emission may still be strong enough for detection. However, for a thermal plasma, the spectral power drops like ν^{-8} at high frequencies, in contrast to observed microwave spectra that show $\nu^{-(0.3...1)}$ for magnetically active stars (Fig. 2).

Instead, the electron population could be *non-thermal*. Electron energy distributions in cosmic sources are often found to follow a power law, and this also holds for solar and stellar microwave flares (Kundu & Shevgaonkar

1985):

$$n(\gamma) = K(\gamma - 1)^{-\delta} \quad (8)$$

There is wide support for this model from estimates of the brightness temperature (e.g., based on the stellar radius, or from resolved interferometric images). The important question then is how these coronae are continuously replenished with high-energy electrons.

The radio-spectral time development implied by this model can be analytically calculated for the case of a short injection of electrons into the corona (Chiuderi Drago & Franciosini 1993). The outline of the derivation is as follows: For trapped electrons with nonthermal number density n , an equation of continuity applies in energy,

$$\frac{\partial n(\gamma, t)}{\partial t} + \frac{\partial}{\partial \gamma} \left[n(\gamma, t) \frac{d\gamma}{dt} \right] = 0 \quad (9)$$

with the solution

$$n(\gamma, t)d\gamma = n(\gamma_0)d\gamma_0. \quad (10)$$

Here, $n(\gamma_0)d\gamma_0$ is the initial distribution. We now need an expression for the energy loss rate of an electron, $d\gamma/dt$. In an extended magnetosphere, the most relevant loss mechanisms are synchrotron loss and Coulomb-collisional loss, given by, respectively,

$$-\dot{\gamma}_{\text{coll}} = 5 \times 10^{-13} n_e \quad [\text{s}^{-1}], \quad \tau_{\text{coll}} = 2 \times 10^{12} \frac{\gamma}{n_e} \quad [\text{s}] \quad (11)$$

$$-\dot{\gamma}_{\text{B}} = 1.5 \times 10^{-9} B^2 \gamma^2 \quad [\text{s}^{-1}], \quad \tau_{\text{B}} = \frac{6.7 \times 10^8}{B^2 \gamma} \quad [\text{s}] \quad (12)$$

(where n_e is the ambient thermal electron density: see, e.g., Petrosian 1985; we have assumed a pitch angle of $\pi/3$). The total energy loss rate is thus

$$\frac{d\gamma}{dt} = \alpha + \beta \gamma^2 \quad (13)$$

with the appropriate coefficients from (11) and (12). This equation has an analytical solution for $n(\gamma, t)$ if the initial distribution is a power law as given by (8), namely

$$n(\gamma, t) = K(1 + \tan^2 A\alpha t) A^\delta \frac{[A\gamma(1 + A \tan A\alpha t) - A + \tan A\alpha t]^{-\delta}}{(1 - A\gamma \tan A\alpha t)^{2-\delta}} \quad (14)$$

where $A = (\beta/\alpha)^{1/2}$, and the initial power-law has been bounded by $\gamma_{0,1} < \gamma_0$ (typically a low energy, e.g., $\gamma_{0,1} = 1.1$) and $\gamma_{0,2} > \gamma_0$, typically a very high energy, formally including $\gamma_{0,2} = \infty$. The evolution of the initial power-law boundaries can be computed; after a finite time, all non-thermal electrons have thermalized. Some characteristic results of these calculations are shown in Fig. 3.

Figure 3a shows the flattening with time of the electron energy distribution due to the collisional losses at lower energies, and a cut-off due to synchrotron losses at higher energies. Figure 3b illustrates the intensity of radiation after calculation of the emissivity and the absorption coefficient, together with an observed spectrum of the RS CVn binary UX Ari. In the early spectrum, the optically thick portion is well visible on the low-frequency side. As the electron energy decays, the spectrum becomes optically thin, and once the high-energy electron population is depleted, the spectrum begins to fall off steeply as there are no electrons left emitting at the observing frequency.

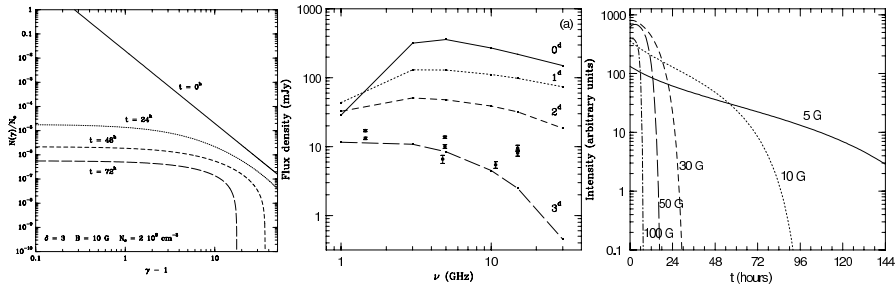


Fig. 3. Time-dependent spectral model of an RS CVn magnetosphere after injection of a power-law electron population. *Left:* Evolution of the electron energy distribution due to collisional and synchrotron losses, starting from a power law. *Middle:* Evolution of the microwave spectrum with time, for a magnetic field of $B = 10$ G and an initial electron power-law index of $\delta = 2$. The electron density in the thermal power-law is $n_e = 2 \times 10^8 \text{ cm}^{-3}$. *Right:* Time evolution of the radiation intensity at 5 GHz, for different magnetic field strength. (From Chiuderi Drago & Franciosini 1993, courtesy of E. Franciosini.)

The time development of the emitted intensity as a function of magnetic field strength (Fig. 3c) shows that the initial radiation originates in fields of higher strength (the “core”), but the responsible electron population decays rapidly due to synchrotron losses. Eventually, radiation from the slowly-decaying population in the weaker, more extended magnetic fields (the “halo”) begins to dominate on longer time scales.

A power-law index of $\delta = 2 - 3$ (as also used above) appears to usually fit active-stellar microwave spectra such as those shown in Fig. 2 quite well (White et al. 1989; Umana et al. 1998). This suggests very hard electron distributions, similar to those seen in gradual solar flares (Cliver et al. 1986). But such distributions are observed during so-called quiescence - an indication that quiescent radio emission is due to a flare-like process? We will return to this hypothesis in later sections.

5 Thermal X-ray emission from stellar coronae

5.1 High-resolution X-ray spectroscopy

The high-resolution X-ray spectrometers on *XMM-Newton* and *Chandra* cover a large range of spectral lines that are temperature- and partly density-sensitive. The spectra thus contain the features required for deriving X-ray emission measure distributions, abundances, coronal densities, and opacities.

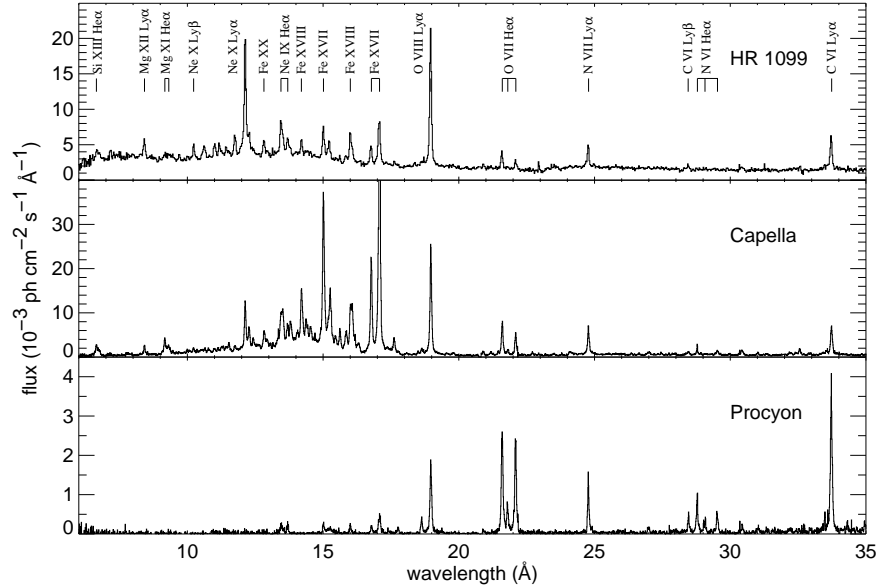


Fig. 4. Three high-resolution X-ray spectra of stars with largely differing activity levels: HR 1099, Capella, and Procyon. Data from *XMM-Newton* RGS.

Figure 4 shows examples of X-ray spectra. The stars cover the entire range of stellar activity: HR 1099 representing a very active RS CVn system, Capella an intermediately active binary, and Procyon an inactive F dwarf. The spectrum of HR 1099 reveals a considerable amount of continuum and comparatively weak lines, which is a consequence of the very hot plasma in this corona ($T \approx 5 - 30$ MK). Note also the unusually strong Ne IX/Fe XVII and Ne X/Fe XVII flux ratios if compared to the other stellar spectra (these ratios are due to an intrinsic compositional anomaly of the HR 1099 corona). The spectrum of Capella is dominated by Fe XVII and Fe XVIII lines which are preferentially formed in this corona's plasma at $T \approx 6$ MK (Fig. 5). Procyon, in contrast, shows essentially no continuum and only very weak lines of Fe. Its spectrum is dominated by the H- and He-like transitions of C, N, and O formed around 1–4 MK. The flux ratios between H- to He-like transitions

are also convenient temperature indicators: The O VIII $\lambda 18.97$ /O VII $\lambda 21.6$ flux ratio, for example, is very large for HR 1099 but drops below unity for Procyon.

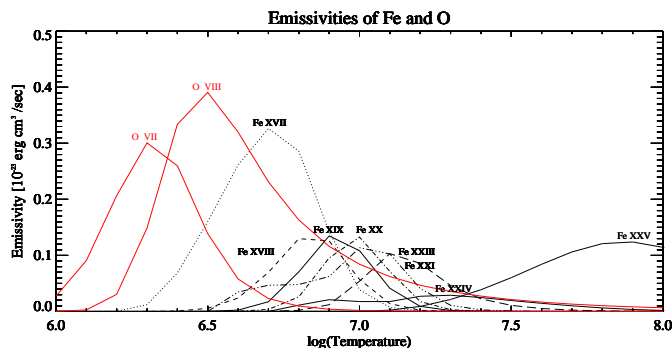


Fig. 5. Emissivities of several X-ray transitions, in particular of highly-ionized iron and oxygen species (Fig. courtesy of A. Telleschi, after Telleschi et al. 2005).

5.2 Thermal coronal components

The large range of temperatures measured in stellar coronae has been a challenge for theoretical interpretation. Whereas much of the solar coronal plasma can be well described by a component of a few million degrees, magnetically active stars have consistently shown a wide distribution of electron temperatures, reaching values as high as 50 MK outside obvious flares.

The flux ϕ_j observed in a spectral line from a given atomic transition can be written as

$$\phi_j = \frac{1}{4\pi d^2} \int AG_j(T) \frac{n_e n_H dV}{d\ln T} \quad (15)$$

where d denotes the distance, and $G_j(T)$ is the “line cooling function” (luminosity per unit EM; Fig. 5) that contains the atomic physics of the transition as well as the ionization fraction for the ionization stage in question, and A is the abundance of the element with respect to some basic tabulation used for G_j . For a fully ionized plasma with cosmic abundances, the hydrogen density $n_H \approx 0.85n_e$. The expression

$$Q(T) = \frac{n_e n_H dV}{d\ln T} \quad (16)$$

defines the *differential emission measure distribution* (DEM). I will use this definition throughout but note that some authors define $Q'(T) = n_e n_H dV/dT$ which is smaller by one power of T . For a plane-parallel atmosphere with surface area S , Eq. (16) implies

$$Q(T) = n_e n_H S H(T), \quad H(T) = \left| \frac{1}{T} \frac{dT}{ds} \right|^{-1} \quad (17)$$

where H is the *temperature scale height*.

5.3 Observational results

“Discrete” (binned) emission measure distributions (EMDs) reflecting the full DEMs can be obtained by various inversion algorithms from the observed spectra. Most EMDs have generally been found to be singly or doubly peaked and confined on either side approximately by power laws (e.g., Schrijver et al. 1995). Interestingly, EMDs are often very steep on the low- T side, and this is particularly true for the more active stars. For example, the slope of the stellar EMD in Fig. 6a follows approximately $Q \propto T^3$ on the low- T side.

It is notable that the complete EMD shifts to higher temperatures with increasing stellar activity as seen in Fig. 6ac, often leaving very little EM at modest temperatures and correspondingly weak spectral lines from ions of C, N, and O.

As a consequence, a relatively tight correlation between the characteristic coronal temperature (e.g., derived from a DEM) and the normalized coronal luminosity L_X/L_{bol} is found: *Stars at higher activity levels support hotter coronae*, with the most active stellar coronae reaching characteristic temperatures of several tens of MK. An example of solar analogs is shown together with the Sun itself during its activity maximum and minimum in Fig. 7. Here,

$$L_X \propto T^{4.5 \pm 0.3} \quad (18)$$

$$EM \propto T^{5.4 \pm 0.6} \quad (19)$$

where L_X denotes the total X-ray luminosity (but EM and T refer to the “hotter” component in standard 2- T fits to *ROSAT* data).

5.4 Interpretation of differential emission measure distributions

Equations (15) and (16) introduce the DEM as the basic interface between the stellar X-ray observation and the model interpretation of the thermal source. It contains information on the plasma temperature and the density-weighted plasma mass that emits X-rays at any given temperature. Although a DEM is often a highly degenerate description of a complex real corona, it provides important constraints on heating theories and on the range of coronal structures that it may describe. *Solar* DEMs can, similarly to the stellar cases, often be approximated by two power laws $Q(T) \propto T^s$ on either side of their peaks (Fig. 6). The Sun has indeed given considerable guidance in physically interpreting the observed stellar DEMs.

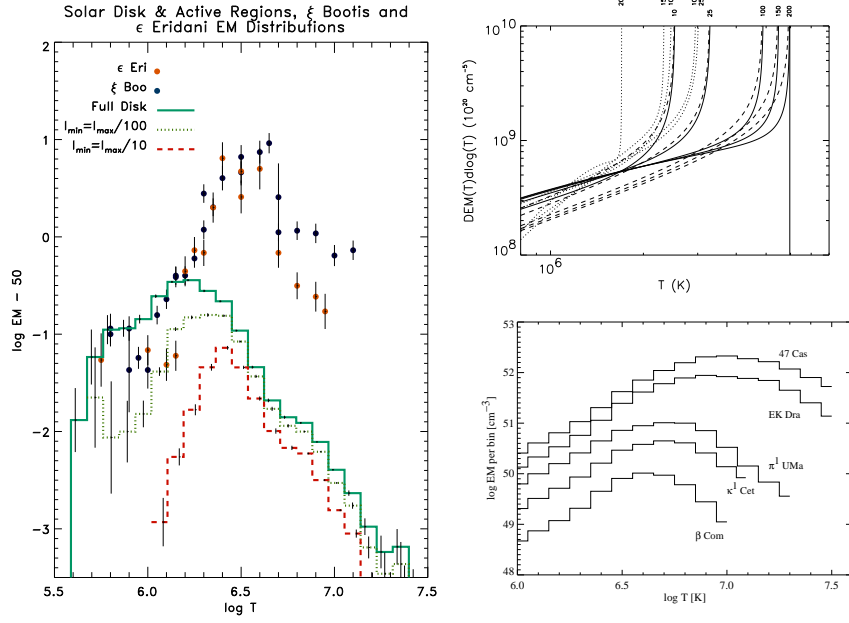


Fig. 6. *Left:* Emission measure distributions of two intermediately active stars (bullets) and the Sun (histograms; EM is in units of 10^{50} cm^{-3}). The histograms refer to full-disk solar EMDs derived from *Yohkoh* images at solar maximum, including also two versions for different lower cutoffs for the intensities in *Yohkoh* images. (figure courtesy of J. Drake, after Drake et al. 2000). – *Upper right:* Calculated differential emission measures of individual static loops. The solid curves refer to uniform heating along the loop and some fixed footpoint heating flux, for different loop half-lengths labeled above the figure panel in megameters. The dashed curves illustrate the analytical solutions presented by Rosner et al. (1978) for uniform heating. The dotted lines show solutions assuming a heating scale height of 2×10^9 cm (figure courtesy of K. Schrijver, after Schrijver & Aschwanden 2002). – *Lower right:* Examples of discrete stellar emission measure distributions of solar analogs (figure courtesy of A. Telleschi).

The DEM of a static loop

The DEM of the plasma contained in a static magnetic loop follows from the hydrostatic equilibrium (see, e.g., derivation by Rosner et al. 1978). Under the conditions of negligible gravity, i.e., constant pressure in the entire loop, and negligible thermal conduction at the footpoints,

$$Q(T) \propto pT^{3/4-\chi/2+\alpha} \frac{1}{\left(1 - [T/T_a]^{2-\chi+\beta}\right)^{1/2}} \quad (20)$$

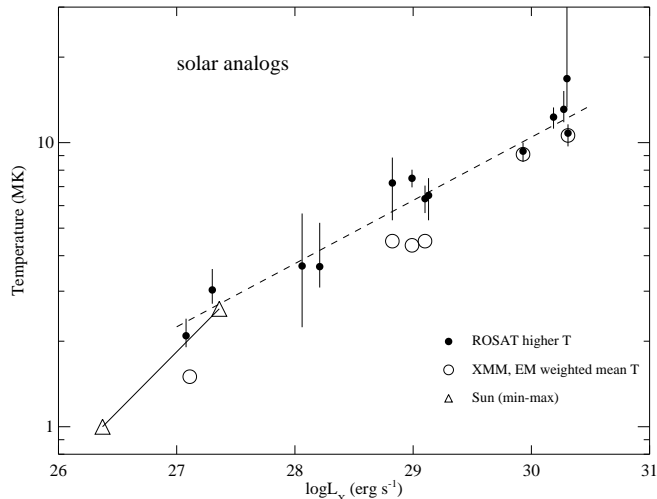


Fig. 7. Coronal temperature vs. X-ray luminosity for solar analogs. For details and references, see Güdel (2004).

(Bray et al. 1991) where T_a is the loop apex temperature, and α and β are power-law indices of, respectively, the loop cross section area S and the heating power q as a function of T : $S(T) = S_0 T^\alpha$, $q(T) = q_0 T^\beta$, and χ is the exponent in the cooling function over the relevant temperature range: $\Lambda(T) \propto T^\chi$. If T is not close to T_a and the loops have constant cross section ($\alpha = 0$), we have

$$Q(T) \propto T^{3/4-\chi/2}, \quad (21)$$

i.e., under typical coronal conditions for non-flaring loops ($T < 10$ MK, $\chi \approx -0.5$), the DEM slope is near unity. If strong thermal conduction is included at the footpoints, then the slope changes to $+3/2$ if not too close to T_a (van den Oord et al. 1997). The single-loop DEM sharply increases at $T \approx T_a$ (Fig. 6).

Loop expansion ($\alpha > 0$) obviously steepens the DEM. Increased heating at the loop footpoints (instead of uniform heating) makes the T range narrower and will also increase the slope of the DEM (see numerical calculations of various loop examples by Schrijver & Aschwanden 2002 and Aschwanden & Schrijver 2002, Fig. 6b).

The DEM of flaring structures

Antiochos (1980) discussed DEMs of solar flaring loops that cool by i) static conduction (without flows), ii) evaporative conduction (including flows), and iii) radiation. The inferred DEMs scale, in the above order, like

$$Q_{\text{cond}} \propto T^{1.5}, \quad Q_{\text{evap}} \propto T^{0.5}, \quad Q_{\text{rad}} \propto T^{-\chi+1}. \quad (22)$$

Since $\chi \approx 0 \pm 0.5$ in the range typically of interest for stellar flares (5–50 MK), all above DEMs are relatively flat (slope 1 ± 0.5). If multiple loops with equal slope but different peak T contribute, then the slope up to the first DEM peak can only become smaller. Non-constant loop cross sections have a very limited influence on the DEM slopes.

Stellar flare observations are often not of sufficient quality to derive temperature and EM characteristics for many different time bins. An interesting diagnostic was presented by Mewe et al. (1997) who calculated the time-integrated (average) DEM of a flare that decays quasi-statically. They find

$$Q \propto T^{19/8} \quad (23)$$

up to a maximum T that is equal to the temperature at the start of the decay phase.

Systems of episodically flaring loops were computed semi-analytically by Cargill (1994), using analytic approximations for conductive and radiative decay phases of the flares. Here, the DEM is defined not by the internal loop structure but by the time evolution of a flaring plasma (assumed to be isothermal). Cargill argued that for radiative cooling, the (statistical) contribution of a flaring loop to the DEM is, to zeroth order, inversely proportional to the radiative decay time, which implies

$$Q(T) \propto T^{-\chi+1} \quad (24)$$

up to a maximum T_m , and a factor of $T^{1/2}$ less if subsonic draining of the cooling loop is allowed. Simulations with a uniform distribution of small flares within a limited energy range agree with these rough predictions, indicating a time-averaged DEM that is relatively flat below 10^6 K but steep ($Q[T] \propto T^4$) up to a few MK, a range in which the cooling function drops rapidly.

Let us next assume - in analogy to solar flares - that the occurrence rate of stellar flares is distributed in energy as a power law with an index α ($dN/dE \propto E^{-\alpha}$). Then, an analytic expression can be derived for the time-averaged DEM of such a flare ensemble, i.e., a “flare-heated corona” (Güdel et al. 2003a). We present a brief outline of the derivation.

Observationally, the flare peak temperature is correlated with the peak EM both in solar (Feldman et al. 1995) and stellar flares (Güdel 2004):

$$\text{EM}_0 = aT_0^b \quad [\text{cm}^{-3}] \quad (25)$$

with $b \approx 4.3 \pm 0.35$ in the range of $T = 10 - 100$ MK (see Fig. 20 further below). The X-ray luminosity L_X of a plasma due to bremsstrahlung and line emission can be expressed as

$$L_X \approx \text{EM} \Lambda(T) = g \text{EM} T^{-\phi} \quad (26)$$

with $\phi \approx 0.3$ over the above temperature range (for broad-band X-ray losses).

From (25) and (26) we obtain a relation between the flare peak temperature T_0 and its peak luminosity $L_{X,0}$,

$$T_0 = \left(\frac{L_{X,0}}{ag} \right)^{1/(b-\phi)}. \quad (27)$$

We will investigate the general case in which τ varies with the flare energy, namely

$$\tau = \tau_0 E^\beta \quad (28)$$

(where $\beta \geq 0$ is assumed, and τ_0 is a constant adjusted to the larger detected flares) in which case

$$\frac{dN}{dL_{X,0}} = \frac{dN}{dE} \frac{dE}{dL_{X,0}} = k' L_{X,0}^{-(\alpha-\beta)/(1-\beta)}. \quad (29)$$

where the constant $k' = k\tau_0^{(1-\alpha)/(1-\beta)}/(1-\beta) > 0$ as long as $\beta < 1$ (which can be reasonably assumed). Since we neglect the short rise time of the flare, our flare light curves are described by their exponential decay at $t \geq 0$,

$$L_X(t) = L_{X,0} e^{-t/\tau}. \quad (30)$$

From hydrodynamic modeling, theory and observations, it is known that during the flare decays $T \propto n_e^\zeta$, where n_e is the plasma density (Reale et al. 1993). The parameter ζ is usually found between 0.5 and 2.

Integrating the above equations for all emission contributions from the decaying and cooling flare plasma over the entire distribution of flares leads to two expressions valid for different regimes:

$$Q(T) \propto \begin{cases} T^{2/\zeta} & \text{for } T < T_m \\ T^{-(b-\phi)(\alpha-2\beta)/(1-\beta)+2b-\phi} & \text{for } T > T_m \end{cases} \quad (31)$$

Here, T_m (a free parameter) is the temperature of the DEM peak. It is controlled by the lower cutoff in the power-law energy distribution of flares (for details, see Güdel et al. 2003a).

5.5 Discussion and summary on the temperature structure

There is, as of yet, no clear explanation for the observed DEMs in active stars. The most notable feature is the often steep slope on the low- T side. The steepness is not easy to explain with standard static loop models, although strong footpoint heating may be a way out. Another explanation are magnetic loops with an expanding cross section from the base to the apex. The larger amount of plasma at high temperatures near the apex evidently steepens the DEM. Solar imaging does not prefer this type of loop, however.

Alternatively, the steep slope may be evidence for continual flaring; equation (31) predicts slopes between 1 and 4, similar to what is often found in magnetically active stars. There is other evidence for this model to have some merit - we will encounter it again in the subsequent sections.

It is also well established that more luminous stars (of a given size) reveal hotter coronae (Fig. 7). Again, the cause of this relation is unclear. Possibly, increased magnetic activity leads to more numerous interactions between adjacent magnetic field structures. The heating efficiency thus increases. In particular, we expect a higher rate of large flares. The increased flare rate produces higher X-ray luminosity because chromospheric evaporation produces more EM; at the same time, the plasma is heated to higher temperatures in larger flares (Güdel et al. 1997).

5.6 Electron densities in stellar coronae

Coronal electron densities control radiative losses from the coronal plasma; observationally, they can in principle also be used in conjunction with EMs to derive approximate coronal source volumes. The spectroscopic derivation of coronal densities is subtle, however. Two principal methods are available.

Densities from Fe line ratios: The emissivities of many transitions of Fe ions in the EUV range are sensitive to densities in the range of interest to coronal research (Mewe et al. 1985). The different density dependencies of different lines of the same Fe ion then also make their *line-flux ratios*, which (apart from blends) are easy to measure, useful diagnostics for the electron density.

Densities from He-like line triplets: The He-like triplets of C V, N VI, O VII, Ne IX, Mg XI, and Si XIII provide another interesting density diagnostic for stellar coronae. Two examples are shown in Fig. 8 (right). The spectra show, in order of increasing wavelength, the resonance, the intercombination, and the forbidden line of the O VII triplet. The corresponding transitions are depicted in the left panel of the Figure. The ratio between the fluxes in the forbidden line and the intercombination line is sensitive to density (Gabriel & Jordan 1969) for the following reason: if the electron collision rate is sufficiently high, ions in the upper level of the forbidden transition, $1s2s\ ^3S_1$, do not return to the ground level, $1s^2\ ^1S_0$, instead the ions are collisionally excited to the upper levels of the intercombination transitions, $1s2p\ ^3P_{1,2}$, from where they decay radiatively to the ground state. They thus enhance the flux in the intercombination line and weaken the flux in the forbidden line. The measured ratio $R = f/i$ of the forbidden to the intercombination line flux can be written as

$$R = \frac{R_0}{1 + n_e/N_c} = \frac{f}{i} \quad (32)$$

where R_0 is the limiting flux ratio at low densities and N_c is the critical density at which R drops to $R_0/2$. The parameters R_0 and N_c are slightly

dependent on the electron temperature in the emitting source. A few useful parameters are collected in Table 2. A systematic problem with He-like triplets is that the critical density N_c increases with the formation temperature of the ion, i.e., higher- Z ions measure only high densities at high T , while the lower-density analysis based on C V, N VI, O VII, and Ne IX is applicable only to cool plasma.

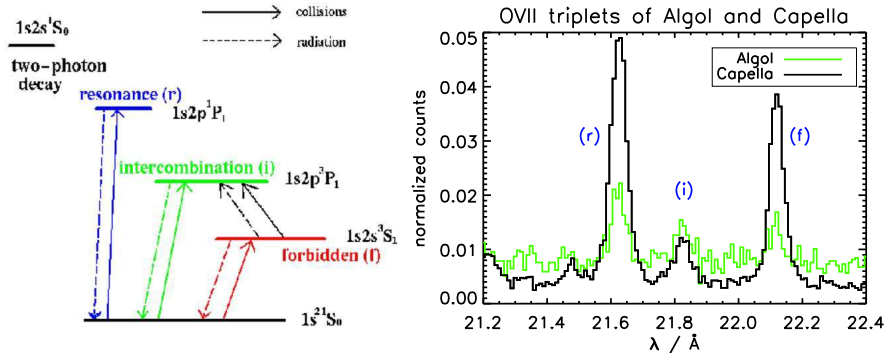


Fig. 8. *Left:* Term diagram for transitions in He-like triplets. The resonance, intercombination, and forbidden transitions are marked. The transition from 3S_1 to 3P_1 re-distributes electrons from the upper level of the forbidden transition to the upper level of the intercombination transition, thus making the f/i line-flux ratio density sensitive. In the presence of a strong UV field, however, the same transition can be induced by radiation as well. *Right:* He-like triplet of O VII for Capella (black) and Algol (green). The resonance (r), intercombination (i), and forbidden (f) lines are marked. The f/i flux ratio of Algol is suppressed probably due to the strong UV radiation field of the primary B star (data from *Chandra*; both figures courtesy of J.-U. Ness).

A review of the literature shows a rather unexpected segregation of coronal densities into two realms at different temperatures. The cool coronal plasma measured by C, N, and O lines in inactive stars is typically found at low, solar-like densities of order $10^9 \text{ cm}^{-3} - 10^{10} \text{ cm}^{-3}$. In *active* stars, the cooler components may show elevated densities up to several times 10^{10} cm^{-3} , but it is the hotter plasma component that apparently reveals extreme values up to $> 10^{13} \text{ cm}^{-3}$ (e.g., Dupree et al. 1993; Schrijver et al. 1995). A basic concern with these latter measurements is that most of the reported densities are only slightly above the low-density limits for the respective ratios, and upper limits have equally been reported, sometimes resulting in conflicting statements for different line ratios in the same spectrum (Ness et al. 2004; Phillips et al. 2001; Osten et al. 2003). Several authors have concluded that the extremely high densities found in some active stars are spurious and perhaps not representative of coronal features. The observational situation is

Table 2. Density-sensitive He-like triplets^a

Ion	$\lambda(r, i, f)$ (Å)	R_0	N_c	$\log n_e$ range ^b	T range ^c (MK)
C V	40.28/40.71/41.46	11.4	6×10^8	7.7–10	0.5–2
N VI	28.79/29.07/29.53	5.3	5.3×10^9	8.7–10.7	0.7–3
O VII	21.60/21.80/22.10	3.74	3.5×10^{10}	9.5–11.5	1.0–4.0
Ne IX	13.45/13.55/13.70	3.08	8.3×10^{11}	11.0–13.0	2.0–8.0
Mg XI	9.17/9.23/9.31	2.66 ^d	1.0×10^{13}	12.0–14.0	3.3–13
Si XIII	6.65/6.68/6.74	2.33 ^d	8.6×10^{13}	13.0–15.0	5.0–20

^adata derived from Porquet et al. (2001) at maximum formation temperature of ion

^brange where R is within approximately [0.1,0.9] times R_0

^crange of 0.5–2 times maximum formation temperature of ion

^dfor measurement with *Chandra* HETGS-MEG spectral resolution

clearly unsatisfactory at the time of writing. The resolution of these contradictions requires a careful reconsideration of atomic physics issues.

6 The structure of stellar coronae

The magnetic structure of stellar coronae is one of the central topics in the stellar coronal research discipline. The extent and predominant locations of magnetic structures currently hold the key to our understanding of the internal magnetic dynamo. All X-ray inferences of coronal magnetic structure in stars other than the Sun are so far indirect, while direct imaging, although at modest resolution, is available at radio wavelengths.

6.1 Magnetic loop models

Closed magnetic loops are the fundamental “building blocks” of the solar corona. When interpreting stellar coronae of any kind, we assume that this concept applies as well, although caution is in order. Even in the solar case, loops come in a wide variety of shapes and sizes (Fig. 9) and appear to imply heating mechanisms and heating locations that are poorly understood - see, for example, Aschwanden et al. (2000). Nevertheless, simplified loop models offer an important starting point for coronal structure studies and possibly for coronal heating diagnostics. A short summary of some elementary properties follows.

Rosner et al. (1978) (RTV) have modeled hydrostatic loops with constant pressure (i.e., the loop height is smaller than the pressure scale height). They also assumed constant cross section, uniform heating, and absence of gravity, and found two scaling laws relating the loop semi-length L (in cm), the volumetric heating rate ϵ (in $\text{erg cm}^{-3}\text{s}^{-1}$), the pressure p (in dynes cm^{-2}), and the loop apex temperature T_a (in K),

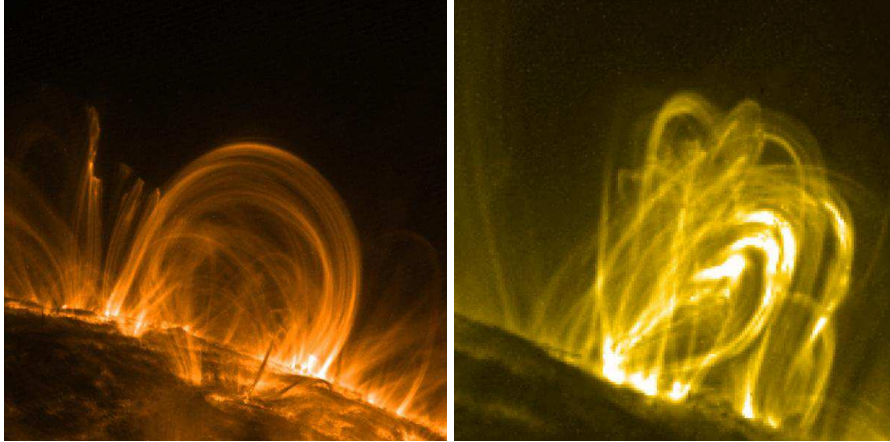


Fig. 9. *Left:* Example of a solar coronal loop system observed by *TRACE*. *Right:* Flaring loop system (observation by *TRACE* at 171Å). Although these images show the emission from relatively cool coronal plasma, they illustrate the possible complexity of magnetic fields.

$$T_a = 1400(pL)^{1/3}; \quad \epsilon = 9.8 \times 10^4 p^{7/6} L^{-5/6}. \quad (33)$$

Serio et al. (1981) extended these scaling laws to loops exceeding the pressure scale height s_p , whereby, however, the limiting height at which the loops grow unstable is $(2 - 3)s_p$:

$$T_a = 1400(pL)^{1/3} e^{-0.04L(2/s_H + 1/s_p)}; \quad \epsilon = 10^5 p^{7/6} L^{-5/6} e^{0.5L(1/s_H - 1/s_p)}. \quad (34)$$

Here, s_H is the heat deposition scale height. For loops with an area expansion factor $\Gamma > 1$, Vesecky et al. (1979) found numerical solutions that approximately follow the scaling laws (Schrijver et al. 1989b)

$$T_a \approx 1400\Gamma^{-0.1}(pL)^{1/3}; \quad T_a = 60\Gamma^{-0.1}L^{4/7}\epsilon^{2/7}. \quad (35)$$

There are serious disagreements between some *solar*-loop observations and the RTV formalism so long as simplified quasi-static heating laws are assumed, the loops being more isothermal than predicted by the models. There is, however, only limited understanding of possible remedies, such as heating that is strongly concentrated at the loop footpoints, or dynamical processes in the loops (see, for example, a summary of this debate in Schrijver & Aschwanden 2002).

6.2 Coronal structure from loop models

When we interpret stellar coronal spectra, we assume, to first order, that some physical loop parameters map on our measured quantities, such as temperature and EM (and possibly density), in a straightforward way. In the simplest

approach, we assume that the observed luminosity L_X is produced by an ensemble of identical coronal loops with characteristic half-length L , surface filling factor f , and an apex temperature T used for the entire loop; then, on using (33) and identifying $L_X = \epsilon V$, we obtain

$$L \approx 6 \times 10^{16} \left(\frac{R_*}{R_\odot} \right)^2 \frac{f}{L_X} T^{3.5} \quad [\text{cm}]. \quad (36)$$

This relation can only hold if L is smaller than the pressure scale height. As an example, for an active solar analog ($R = R_\odot$, $L_X = 10^{30} \text{ erg s}^{-1}$, $T = 10^7 \text{ K}$) we obtain $L \approx 2 \times 10^{11} f \text{ cm}$. The coronal volume is approximately $V \approx 8R^2 f L$ and the electron density $n_e = (EM/V)^{1/2}$. Further, $L_X \approx 2 \times 10^{-23} EM \text{ erg s}^{-1}$. For the solar analog, thus, we find $n_e f \approx 2.5 \times 10^9 \text{ cm}^{-3}$. The luminous, hot plasma component in magnetically active stars therefore seems to invariably require either very large, moderate-pressure loops with a large filling factor, or solar-sized high-pressure compact loops with a very small ($\lesssim 1\%$) filling factor.

While the above interpretational work identifies spectral-fit parameters such as T or EMs with parameters of theoretical loop models, a physically more appealing approach involves full hydrostatic models whose calculated emission spectra are directly fitted to the observations.

Such studies (Stern et al. 1986; Giampapa et al. 1996; Maggio & Peres 1997; Ventura et al. 1998) have found that the cooler component at $\approx 1 - 2 \text{ MK}$ requires loops of small length ($L \ll R_*$) but high pressure ($p > p_\odot$), whereas the high- T component at $\approx 5 - 10 \text{ MK}$ must be confined by very compact loops with extremely high base pressures (up to hundreds of dynes cm^{-2}) and small ($< 1\%$) filling factors. These parameters are suspiciously “flare-like” - the observed hot plasma is perhaps indeed related to multiple, very compact flaring regions.

The most essential conclusion from these exercises is perhaps that, within the framework of such simplistic models, the loop heating rate required for magnetically active stars may exceed values for typical solar loops by orders of magnitude, pointing toward some enhanced heating process reminiscent of the energy deposition in flares. The compactness of the hot loops and the consequent high pressures also set these coronal structures clearly apart from any non-flaring solar coronal features.

6.3 Coronal structure from densities

Spectroscopically measured densities provide, in conjunction with EMs, important estimates of emitting volumes. If the trend suggested from density-sensitive line flux ratios holds, namely that for increasing temperature, the pressures become progressively higher, then progressively smaller volumes are a consequence. The volume required for a luminosity of $10^{30} \text{ erg s}^{-1}$ at 10 MK is $V = L_X / (2 \times 10^{-23} n_e^2) \text{ cm}^{-3} = 5 \times 10^{26} \text{ cm}^{-3}$ (where the coefficient

2×10^{-23} is from (5), appropriate for $T = 10$ MK), corresponding to a layer of only 80 m height around a solar-like star, or 8 km for a filling factor of only 1%! Such scales are much smaller than chromospheric scale height and therefore problematic. Still smaller filling factors must be assumed for a star of this kind. Similarly, from the RTV loop scaling law (33) - if applicable -, a loop height $h = 2L/\pi = 8.5 \times 10^5 T^2/n_e \approx 80$ km is found, again an unreasonably small size.

The confinement of plasma at such high densities in compact sources would also require coronal magnetic field strengths of order $B > (16\pi n_e kT)^{1/2} \approx 1$ kG, i.e., field strengths like those very close and just above (sun-)spots. In that case, the typical magnetic dissipation time is only a few seconds for $n_e \approx 10^{13} \text{ cm}^{-3}$ if the energy is derived from the same magnetic fields, suggesting that the small, bright loops light up only briefly. In other words, the stellar corona would be made up of numerous ephemeral loop sources that cannot be treated as being in a quasi-static equilibrium (van den Oord et al. 1997).

6.4 X-ray coronal imaging: Overview

X-ray images of stellar coronae have been derived from eclipses in binaries, or from rotational modulation in rapidly rotating stars. We keep in mind that any indirect imaging of this kind is highly biased by observational constraints (e.g., the volume that is subject to eclipses or self-eclipses, or the accessible temperature range) and by the amount and density of plasma trapped in the magnetic fields. X-ray imaging captures strongly emitting plasma, *not* the entire magnetic-field structure.

The “image” to be reconstructed consists of volume elements at coordinates (x, y, z) with *optically thin* fluxes $f(x, y, z)$ assumed to be constant in time. In the special case of negligible stellar rotation during the observation, the problem can be reduced to a 2-D projection onto the plane of the sky, at the cost of positional information along the line of sight (Fig. 10). In general, one thus seeks the geometric brightness distribution $f(x, y, z) = f_{ijk}$ (i, j, k being the discrete number indices of the volume elements) from a binned, observed light curve $F_s = F(t_s)$ that undergoes a modulation due to an eclipse or due to rotation.

6.5 Active-region modeling

In the most basic approach, the emitting X-ray or radio corona can be modeled by making use of a small number of simple, elementary building blocks that are essentially described by their size, their brightness, and their location. This approach is the 3-D equivalent to standard surface spot modeling. Preferred building block shapes are radially directed, uniformly bright, optically thin, radially truncated spherical cones with their apexes at the stellar

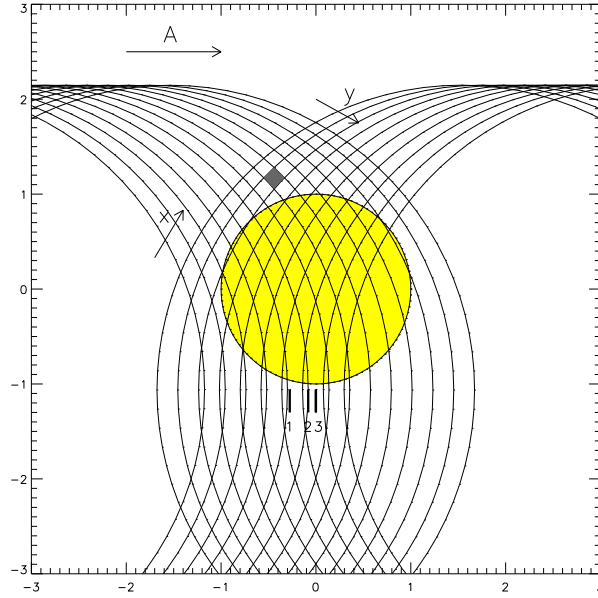


Fig. 10. Sketch showing the geometry of an eclipsing binary (in this case, α CrB, figure from Güdel et al. 2003b). The large circles illustrate the limbs of the eclipsing star that moves from left to right in front of the eclipsed star (shown in yellow). The limbs projected at different times during ingress and egress define a distorted 2-D array (x, y) of pixels (an example of a pixel is shown in gray).

center. Free parameters are their opening angles, their heights above the stellar surface, their radiances, and their central latitudes and longitudes. These parameters are then varied until the model fits the observed light curve.

A minimum solution can be found for a rotationally modulated star (Güdel & Schmitt 1995). If a rotationally modulated feature is *invisible* during a phase interval φ of the stellar rotation, then all sources contributing to this feature must be confined to within a maximum volume, V_{\max} , given by

$$\frac{V_{\max}}{R_*^3} = \frac{\psi}{3} - \frac{(2\pi - \varphi)(1 + \sin^2 i)}{6\sin i} + \frac{2\cot(\chi/2)}{3\tan i} \quad (37)$$

where $\tan\chi = \tan(\varphi/2)\cos i$, $\sin(\psi/2) = \sin(\varphi/2)\sin i$ with $0 \leq \psi/2 \leq \pi/2$, and χ and $\varphi/2$ lie in the same quadrant (i is the stellar inclination, $0 \leq i \leq \pi/2$). Together with the modulated fraction of the luminosity, lower limits to average electron densities in the modulated region follow directly.

6.6 Maximum-entropy image reconstruction

Maximum entropy methods (MEM) are applicable both to rotationally modulated light curves and to eclipse observations. The standard MEM selects among all images f_{ijk} (defined in units of counts per volume element) that are compatible with the observation, the one that minimizes the Kullback contrast (“relative entropy”)

$$K = \sum_{i,j,k} f_{ijk} \ln \frac{f_{ijk}}{f_{ijk}^a} \quad (38)$$

with respect to an a priori image f_{ijk}^a , which is usually unity inside the allowed area or volume and vanishes where no brightness is admitted. Minimizing K thus introduces the least possible information while being compatible with the observation. The contrast K is minimum if f_{ijk} is proportional to f_{ijk}^a and thus flat inside the field of view, and it is maximum if the whole flux is concentrated in a single pixel (i, j, k) . The compatibility with the observed count light curve is measured by χ^2 ,

$$\chi^2 = \sum_s \frac{(F_s^* - F_s)^2}{F_s^*} \quad (39)$$

where F_s and F_s^* are, respectively, the observed number of counts and the number of counts predicted from f_{ijk} and the eclipse geometry. Poisson statistics usually requires more than 15 counts per bin. Finally, normalization is enforced by means of the constraint

$$N = \frac{\left(f^{\text{tot}} - \sum_{ijk} f_{ijk} \right)^2}{f^{\text{tot}}} \quad (40)$$

where f^{tot} is the sum of all fluxes in the model.

The final algorithm minimizes the cost function

$$C = \chi^2 + \xi K + \eta N. \quad (41)$$

The trade-off between the compatibility with the observation, normalization, and unbiasedness is determined by the Lagrange multipliers ξ and η such that the reduced χ^2 is $\lesssim 1$, and normalization holds within a few percent.

6.7 Lucy/Withbroe image reconstruction

This method (after Lucy 1974 and Withbroe 1975) iteratively adjusts fluxes in a given set of volume elements based on the mismatch between the model and the observed light curves in all time bins to which the volume element

contributes. At any given time t_s during the eclipse, the observed flux F_s is the sum of the fluxes f_{ijk} from all volume elements that are unocculted:

$$F(t_s) = \sum_{i,j,k} f_{ijk} \mathbf{m}_s(i, j, k) \quad (42)$$

where \mathbf{m}_s is the ‘‘occultation matrix’’ for the time t_s : it puts, for any given time t_s , a weight of unity to all visible volume elements and zero to all invisible elements (and intermediate values for partially occulted elements). Since F_s is given, one needs to solve (42) for the flux distribution, which is done iteratively as follows:

$$f_{ijk}^{n+1} = f_{ijk}^n \frac{\sum_s \frac{F_o(t_s)}{F_m^n(t_s)} \mathbf{m}_s(i, j, k)}{\sum_s \mathbf{m}_s(i, j, k)} \quad (43)$$

where $F_o(t_s)$ and $F_m^n(t_s)$ are, respectively, the observed flux and the model flux (or counts) in the bin at time t_s , both for the iteration step n . Initially, a plausible, smooth distribution of flux is assumed, e.g., constant brightness, or some r^{-p} radial dependence.

6.8 Backprojection and Clean image reconstruction

If rotation can be neglected during an eclipse, for example in long-period detached binaries, then the limb of the eclipsing star is projected at regular time intervals onto the plane of the sky and therefore onto a specific part of the eclipsed corona, first during ingress, later during egress (Güdel et al. 2003b). The two limb sets define a 2-D grid of distorted, curved pixels (Fig. 10). The brightness decrement during ingress or, respectively, the brightness increment during egress within a time step $[t_s, t_{s+1}]$ originates from within a region confined by the two respective limb projections at t_s and t_{s+1} . Ingress and egress thus each define a 1-D image by backprojection from the light curve gradients onto the plane of the sky. The relevant reconstruction problem from multiple geometric projections is known in tomography. The limiting case of only two independent projections can be augmented by a CLEAN step, as follows. The pixel with the largest *sum* of projected fluxes from ingress and egress is assumed to represent the location of a real source. A fraction, $g < 1$, of this source flux is then subtracted from the two projections and saved on a clean map, and the process is iterated until all flux is transferred onto the latter.

6.9 X-ray coronal structure inferred from eclipses

Extent of eclipsed coronal features

Some shallow X-ray eclipses in tidally interacting binary systems of the RS CVn, Algol, or BY Dra type have provided important information on extended coronal structure. For example, Walter et al. (1983) concluded that

the coronae in the AR Lac binary components are bi-modal in size, consisting of compact, high-pressure (i.e., 50–100 dynes cm^{-2}) active regions with a scale height $< R_*$, while the subgiant K star is additionally surrounded by an extended ($2.7R_*$) low-pressure corona. Further, a hot component pervading the entire binary system was implied from the absence of an eclipse in the hard ME detector on *EXOSAT* (White et al. 1990), and similar conclusions have been drawn from detailed light-curve inversion analysis (Preš et al. 1995).

X-ray dips or any periodic modulation have often been absent in X-ray observations of binaries. This again has been taken as evidence of a very extended (about $1R_*$ in the case of Algol, White et al. 1986) X-ray corona unless more compact structures sit at high latitudes where they remain uneclipsed.

Among wide, non-interacting eclipsing stars, α CrB provides a particularly well-suited example because its X-ray active, young solar analog (G5 V) is totally eclipsed every 17 days by the optical primary, an A0 V star that is perfectly X-ray dark. Other parameters are ideal as well, such as the non-central eclipse, the eclipse time-scale of a few hours, and the relatively slow rotation period of the secondary. Image reconstructions from eclipse observations (Güdel et al. 2003b) reveal patches of active regions across the face of the G star; not much material is found significantly beyond its limb (Fig. 12). The structures tend to be of modest size ($\approx 5 \times 10^9$ cm), with large, X-ray faint areas in between, although the star’s luminosity exceeds that of the active Sun by a factor of ≈ 30 . These observations imply moderately high densities in the emitting active regions, reaching a few 10^{10} cm^{-3} in the brightest active regions.

6.10 Eclipsed X-ray flares

Eclipses of flares have contributed very valuable information on densities and the geometric size of flaring structures. Only few reports are available, among them the following:

Choi & Dotani (1998) described a full eclipse of an X-ray flare in progress in the contact binary system VW Cep. During a narrow dip in the flare decay, the X-ray flux returned essentially to the pre-flare level. Geometric considerations then placed the flare near one of the poles of the primary star, with a size scale of order 5.5×10^{10} cm or somewhat smaller than the secondary star. The authors consequently inferred an electron density of $5 \times 10^{10} \text{ cm}^{-3}$. A polar location was also advocated for a flare on Algol observed across an eclipse by Schmitt & Favata (1999). The flare emission was again eclipsed completely, and judged from the known system geometry, the flare was located above one of the poles, with a maximum source height of no more than approximately $0.5R_*$, implying a minimum electron density of $9.4 \times 10^{10} \text{ cm}^{-3}$ if the volume filling factor was unity. A more moderate flare was observed during an eclipse in the Algol system by Schmitt et al.

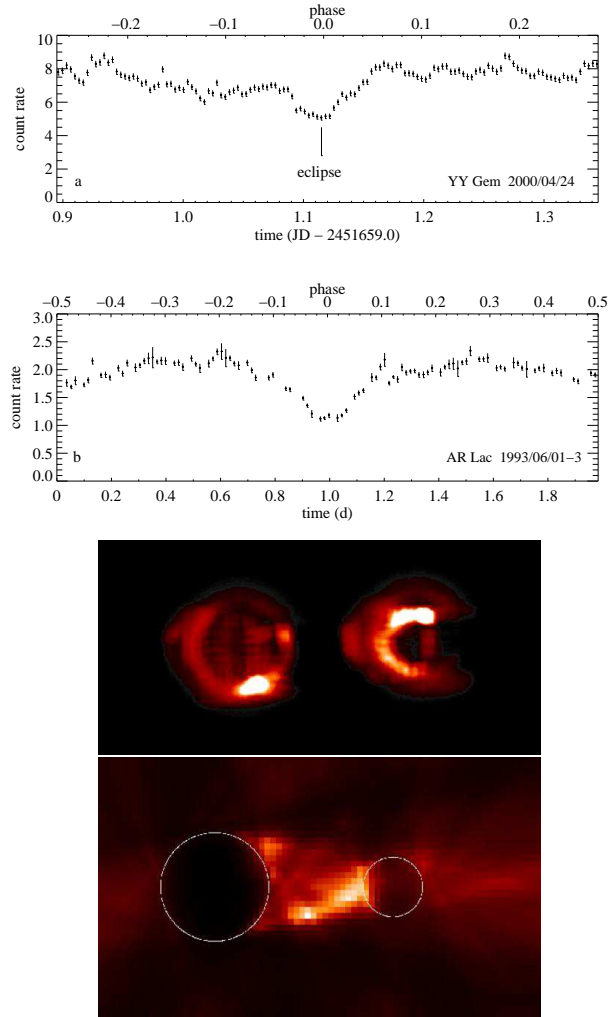


Fig. 11. Two examples of eclipses and the corresponding coronal image reconstructions. *From top to bottom:* Light curve of the YY Gem system (from Güdel et al. 2001a, observation with *XMM-Newton* EPIC); light curve of the AR Lac system (after Siarkowski et al. 1996, observation with *ASCA* SIS); reconstructed image of the coronal structure of, respectively, YY Gem (at phase 0.375) and AR Lac (at quadrature). The latter figure shows a solution with intrabinary emission. (The light curve of AR Lac is phase-folded; the actual observation started around phase 0; data and image for AR Lac courtesy of M. Siarkowski.)

(2003). In this case, the image reconstruction required an equatorial location, with a compact flare source of height $h \approx 0.1R_*$. Most of the source volume

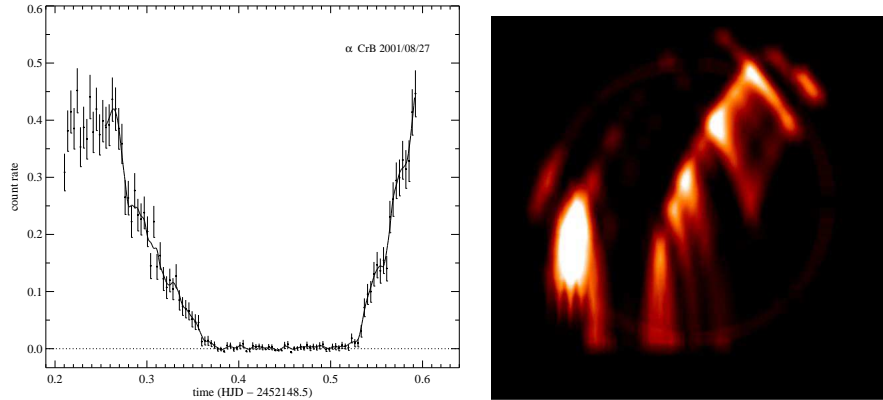


Fig. 12. Light curve and image reconstruction of the A+G binary α CrB. The left panel shows the light curve from observations with *XMM-Newton*, the right panel illustrates the reconstructed X-ray brightness distribution on the G star (after Güdel et al. 2003b).

exceeded densities of 10^{11} cm^{-3} , with the highest values at $\approx 2 \times 10^{11} \text{ cm}^{-3}$. Because the *quiescent* flux level was attained throughout the flare eclipse, the authors argued that its source, in turn, must be concentrated near the polar region with a modest filling factor of $f < 0.1$ and electron densities of $\approx 3 \times 10^{10} \text{ cm}^{-3}$.

6.11 Radio Very Long Baseline Interferometry

By interferometrically combining radio telescopes over large distances, angular resolutions of as little as one milliarcsecond can be achieved in the microwave range.

VLBI techniques have been very demanding for single late-type dwarf stars, owing both to low flux levels and small coronal sizes. Some observations with mas angular resolutions show unresolved quiescent or flaring sources, thus constraining the brightness temperature to $T_b > 10^{10} \text{ K}$ (e.g., Benz et al. 1995), whereas others show evidence for extended coronae with coronal sizes up to several times the stellar size.

The dMe star UV Cet was found to be surrounded by a pair of giant synchrotron lobes, with sizes up to $2.4 \times 10^{10} \text{ cm}$ and a separation of 4–5 stellar radii along the putative rotation axis of the star, suggesting very extended magnetic structures above the magnetic poles (Fig. 13a), perhaps arranged in a global dipole as sketched in Fig. 15b. I discuss this observation in some detail, following Benz et al. (1998), to demonstrate the procedures with which we can characterize the magnetic field structure. Throughout, we assume, as detailed further above, that the emission is optically thin gyrosynchrotron

emission from a power-law population of accelerated electrons with a number density distribution in energy ϵ

$$n(\epsilon) = N(\delta - 1)\epsilon_0^{\delta-1}\epsilon^{-\delta} \quad [\text{cm}^{-3}\text{erg}^{-1}] \quad (44)$$

where $\epsilon = (\gamma - 1)m_e c^2$ is the kinetic particle energy, γ is the Lorentz factor, and $\delta > 1$ has been assumed so that N is the total non-thermal electron number density above ϵ_0 .

We first need an expression for the emissivity: For isotropic pitch angle electron distributions according to (44) with $2 \lesssim \delta \lesssim 7$, for harmonics $10 \lesssim s \lesssim 100$, and for the x-mode (Dulk 1985)

$$\eta_\nu \approx 3.3 \times 10^{-24} B N 10^{-0.52\delta} (\sin \theta)^{-0.43+0.65\delta} \left(\frac{\nu}{\nu_c} \right)^{1.22-0.90\delta} \quad (45)$$

(in $\text{erg s}^{-1} \text{cm}^{-3} \text{Hz}^{-1} \text{sterad}^{-1}$). Here, θ denotes the emission angle to the magnetic field, and $\nu_c = eB/m_e c$ is the electron gyrofrequency. The coefficient of this expression is applicable if a power-law cutoff has been set at 10 keV. This cut-off itself is of little relevance for gyrosynchrotron emission since electrons radiate little at such low energies.

We assume $\theta = \pi/2$ and $\delta \approx 2.5$ (the latter from modeling of M dwarf spectra, Sect. 4.3). Adding o- and x-mode (which have similar emissivities), the intensity is

$$I \approx 1.8\eta_\nu D \quad (46)$$

which is to be compared with the observed intensity of $3.9 \times 10^{-8} \text{erg}^{-1} \text{cm}^{-2} \text{Hz}^{-1} \text{sterad}^{-1}$. Here, the fitted diameter of one of the radio blobs (0.3 milliarcsec or $D = 1.2 \times 10^{10} \text{cm}$) was used. Combining (45)–(46), we find

$$B \approx 2 \times 10^5 N^{-1/2}. \quad (47)$$

This relation is shown in Fig. 13b together with the condition that the particle pressure in the magnetic loops is less than the magnetic pressure,

$$N\bar{\epsilon} \leq \frac{B^2}{8\pi}. \quad (48)$$

We find a lower limit to B of approximately 15 G and an upper limit to N of about $2 \times 10^8 \text{cm}^{-3}$.

At least part of the observed emission was slowly decaying, with a decay timescale of $\tau = 6650 \text{s}$ (perhaps from a flare that filled the magnetospheric volume with electrons). Given the large size of the structure, the dominant energy decay process is likely to be due to synchrotron radiation loss (12). The average frequency of synchrotron emission can be expressed as

$$\bar{\nu} = 1.3 \times 10^6 B \gamma^2 \quad [\text{Hz}] \quad (49)$$

(Melrose 1980). Using the observing frequency (8.4 GHz in this case) for $\bar{\nu}$, we find the decay time

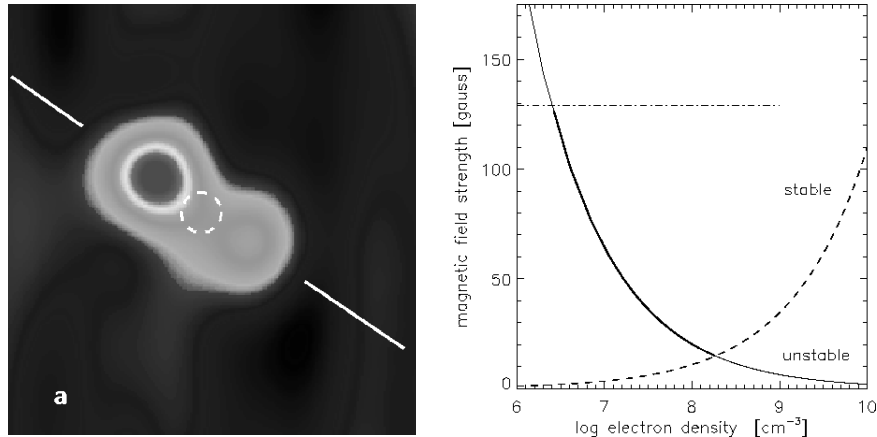


Fig. 13. (a) VLBA image of the dMe star UV Cet; the two radio lobes are separated by about 1.4 mas, while the best angular resolution reaches 0.7 mas. The straight line shows the orientation of the putative rotation axis, assumed to be parallel to the axis of the orbit of UV Cet around the nearby Gl 65 A. The small circle gives the photospheric diameter to size, although the precise position is unknown (after Benz et al 1998). (b) Estimates of the magnetic field and the nonthermal electron density for the same observation (see text for details).

$$\tau = \frac{\gamma}{\dot{\gamma}} \approx 8 \times 10^6 B^{-3/2} \quad [\text{s}] \quad (50)$$

and therefore $B = 113$ G. This defines an upper limit to the magnetic field strength because we have ignored other energy losses that might be present. The upper limit is also drawn in Fig. 13b. We have thus confined the magnetic field strength in the source to 15–130 G.

VLBA imaging and polarimetry of Algol reveals a similar picture with two oppositely polarized radio lobes separated along a line perpendicular to the orbital plane by more than the diameter of the K star (Mutel et al. 1998, Fig. 14 and Fig. 15b). Large-scale polarization structure further supports models that assume globally organized magnetic fields around active binary stars (Beasley & Güdel 2000).

An important, early VLBI result for RS CVn and Algol-like binaries is evidence for a compact core plus extended halo radio structure of a total size that is comparable to the binary system size (Mutel et al. 1985). The basic idea here is the following: During quiescence, an optically thin, very large magnetosphere is filled with a power-law distribution of electrons. The emission is essentially optically thin, with a flat radio spectrum. During an outburst, an active region injects a larger electron population into magnetic loops. The compact source (the “core”), unresolved by VLBI, becomes optically thick due to synchrotron self-absorption, and the radio spectral index consequently becomes positive, and the brightness temperature is thus

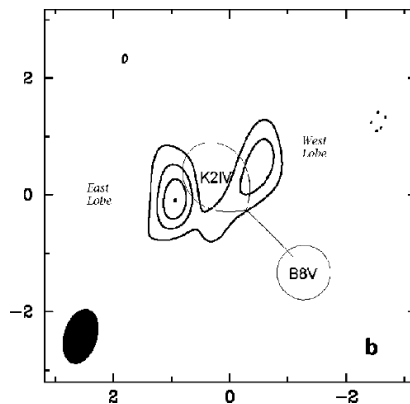


Fig. 14. VLBA observation of Algol at 8.4 GHz, resolving two lobes around the binary. The most likely configuration of the binary components is also drawn (after Mutel et al. 1998).

equal to the effective electron temperature. Mutel et al. (1985) measured a few times 10^{10} K for outbursts on RS CVn-type binaries. Once the electron injection has ceased, the lifetime of the energetic electron population is determined essentially by the synchrotron loss time. The final phase consists of magnetic-loop expansion owing to buoyancy, expanding the source until it merges with the pre-flare “halo” component. At the same time, the source becomes progressively more optically thin, developing a negative radio spectral index and mild circular polarization. Given the large size, the strength of the extended magnetic field must be rather moderate, of order 10 G. To emit radiation at frequency ν in the microwave range, high Lorentz factors are required. Because the spectral power for synchrotron emission is predominantly emitted at a harmonic of order γ^3 of the relativistic gyrofrequency

$$\nu_c = \frac{eB}{m_e \gamma c} = 2.8 \times 10^6 \frac{B}{\gamma}, \quad (51)$$

we require $\gamma \approx 6 \times 10^{-4}(\nu/B)^{1/2}$. For an observing frequency of 5 GHz thus, $\gamma \approx 10$. A model calculation of the spectral development of the microwave radiation was outlined in Sect. 4.3.

6.12 Radio magnetospheric models

VLBI observations of RS CVn and Algol binaries, T Tau stars, and magnetic Bp/Ap stars have shown some perplexing structures with sizes at least as large as the binary system, with polarization properties that suggest that the magnetic fields are globally ordered. This has led to a series of large-scale magnetic models for such systems. They have in common a global, dipole-like structure somewhat resembling the Earth’s Van Allen belts (Fig. 15a).

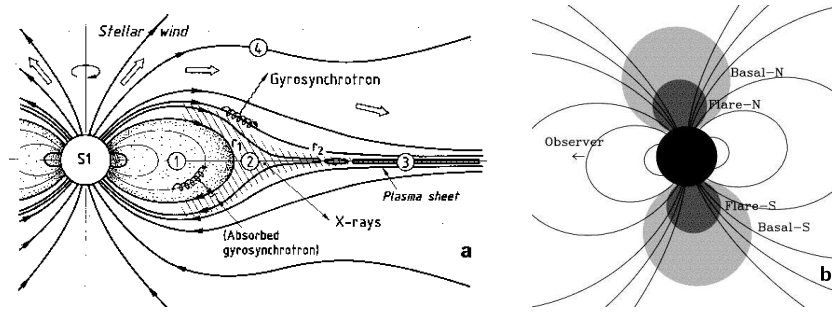


Fig. 15. (a) Equatorial model for the magnetosphere of the young B star S1 in ρ Oph (André et al. 1988). (b) Sketch for radio emission from a global dipole consistent with the VLBI observation shown in Fig. 13b (Mutel et al. 1998; reproduced with permission of the AAS.)

Stellar winds escaping along magnetic fields draw the field lines into a current sheet configuration in the equatorial plane. Particles can be accelerated in that region. They subsequently travel back to become trapped in the dipolar-like, equatorial magnetospheric cavity. Variants of this radiation-belt model, partly based on theoretical work of Havnes & Goertz (1984), have been applied to RS CVn binaries (e.g., Morris et al. 1990), in an optically thick version to Bp/Ap stars (Drake et al. 1987; Linsky et al. 1992) and in an optically thin version to a young B star (André et al. 1988).

Polarization observations of RS CVn binaries support these models. The polarization degree seems to be anticorrelated with the luminosity for any given system, but the sense of polarization changes between lower and higher frequencies. For the entire binary sample, the polarization degree is inversely correlated with the stellar inclination angle such that low-inclination (“pole-on”) systems show the strongest polarization degrees, as expected from such global systems (Mutel et al. 1987, 1998; Morris et al. 1990).

Flares still appear to originate in compact sources within such magnetospheres, probably close to the star. The “core plus halo” model then correctly describes the radio spectral properties - the halo corresponds to the extended magnetosphere. This is also supported by magnetic fields inferred to be stronger (80–200 G) in the flaring core and weaker (10–30 G) in the halo (Umana et al. 1993, 1999; Mutel et al. 1998; Trigilio et al. 2001). Because the optical depth is frequency-dependent, the source is small at high frequencies (with a size $\approx R_*$, above 10 GHz) and large at small frequencies (with a size comparable to the binary system size at 1.4 GHz; Klein & Chiuderi-Drago 1987; Jones et al. 1995). This effect explains the relatively flat, optically thick radio spectra seen during flares.

6.13 Extended or compact coronae?

As the previous discussions imply, we are confronted with mixed evidence for predominantly extended (source height $> R_*$) and predominantly compact ($\ll R_*$) coronal structures or a mixture thereof, results that variably come from radio or from X-ray astronomical observations. There does not seem to be unequivocal agreement on the type of structure that generally prevails. Several trends can be recognized, however, as summarized below.

Compact coronal structure. Steep (portions of the) ingress and egress light curves or prominent rotational modulation unambiguously argue in favor of short scale lengths perpendicular to the line of sight. Common to all are relatively high inferred densities ($\approx 10^{10} \text{ cm}^{-3}$). The pressures of such active regions may exceed pressures of non-flaring solar active regions by up to two orders of magnitude. Spectroscopic observations of high densities and loop modeling add further evidence for the presence of some rather compact sources. Flare modeling also provides modest sizes, often of order $0.1\text{--}1R_*$, for the involved magnetic loops (Sect. 8).

Extended structure. Here, the arguments are less direct and are usually based on the absence of deep eclipses, or very shallow ingress and egress curves. Caution is in order in cases where the sources may be located near one of the polar regions; in those cases, eclipses and rotational modulation may also be absent regardless of the source size. Complementary information is available from flare analysis (see Sect. 8) that in some cases does suggest quite large loops. The caveat here is that simple single-loop models may not apply to such flares. Clear evidence is available from radio interferometry that proves the presence of large-scale, globally ordered magnetic fields. The existence of prominent extended, closed magnetic fields on scales $> R_*$ is therefore *also* beyond doubt for several active stars.

The most likely answer to the question on coronal structure size is therefore an equivocal one: Coronal magnetic structures follow a size distribution from very compact to extended ($\gtrsim R_*$) with various characteristic densities, temperatures, non-thermal electron densities, and surface locations. Quite different loop systems may be responsible when measuring cool X-ray lines or hot lines, or when observing in the microwave range. This is no different from what we see on the Sun even though various features observed on magnetically active stars stretch the comparison perhaps rather too far for comfort.

7 Stellar radio flares

Flares arise as a consequence of a sudden energy release and relaxation process of the magnetic field in solar and stellar coronae. Present-day models assume that the energy is accumulated and stored in non-potential magnetic

fields prior to an instability that most likely implies reconnection of neighboring antiparallel magnetic fields. The energy is brought into the corona by turbulent footpoint motions that tangle the field lines at larger heights. The explosive energy release becomes measurable across the electromagnetic spectrum and, in the solar case, as high-energy particles in interplanetary space as well.

Flares are ubiquitous among coronal stars of all types, with very few exceptions. They have, of course, prominently figured in solar studies, and it is once again solar physics that has paved the way to the interpretation of stellar flares, even if not all features are fully understood yet. The complexity that flares reveal to the solar astronomer is inaccessible in stellar flares, especially in the absence of spatially resolved observations. Simplified concepts, perhaps tested for solar examples, must suffice. The following sections summarize the “stellar astronomer’s way” of looking at flares.

7.1 Incoherent radio bursts

Active stars reveal two principal flare types at radio wavelengths, similar to the solar case:

Incoherent flares evolve on time scales of minutes to hours, they show broad-band spectra and moderate degrees of polarization. These bursts are fully equivalent to solar microwave bursts. Like the latter, they show evidence for the presence of mildly relativistic electrons. The emission is therefore interpreted as gyrosynchrotron radiation from coronal magnetic fields. Many flares on single F/G/K stars are of this type, as are almost all radio flares on M dwarfs above 5 GHz (Bastian 1990), or on RS CVn binaries (Mutel et al. 1985).

7.2 Coherent radio bursts

The stellar equivalents to coherent solar radio bursts (showing high brightness temperature, short durations, perhaps small bandwidth, and perhaps high polarization degree) have been observed already in the early days of radio astronomy, given their sometimes extremely high fluxes. Like for the Sun, they come in a bewildering variety which has made a clear identification of the ultimate cause difficult (Bastian et al. 1998). Coherent bursts are frequent on late-type main-sequence stars, but have also been reported from RS CVn binaries (White & Franciosini 1995).

Such bursts carry important information in high-time resolution light curves. Radio “spike” rise times as short as 5–20 ms have been reported, requiring, from the light-time argument, source sizes of $R < c\Delta t \approx 1500$ –6000 km. With

$$S = \frac{2kT_b\nu^2}{c^2} \frac{\pi R^2}{d^2} \quad (52)$$

and measured fluxes up to 1 mJy for sources at a distance of a few parsec, we derive brightness temperatures of order $T_b \approx 10^{16}$ K, a clear proof of the presence of a coherent mechanism (Lang et al. 1983; Lang & Willson 1986; Güdel et al. 1989a; Bastian et al. 1990).

7.3 Radio dynamic spectra

The standard means to study solar coherent bursts are “dynamic spectra” (flux vs. frequency and time). If the elementary frequencies relevant for the coherent emission process, ν_p and ν_c , evolve in the source, or if the radiating source itself travels across density or magnetic field gradients, the emission leaves characteristic traces on the dynamic spectrum (Bastian et al. 1998). The study of drifts, decay times, harmonic structures etc. may then help identify the emission process and thus infer magnetic field strengths, electron densities, electron energies and beam velocities etc.

Applying the same technology to stellar observations has turned out to be extremely challenging, and only few successful dynamic spectra have been recorded to date. A rich phenomenology has been uncovered, including: a) short, highly polarized bursts with structures as narrow as $\Delta\nu/\nu = 0.2\%$ suggesting either plasma emission from a source of size $\sim 3 \times 10^8$ cm, or a cyclotron maser in magnetic fields of ~ 250 G (Bastian & Bookbinder 1987; Güdel et al. 1989a; Bastian et al. 1990). b) Evidence for spectral structure with positive drift rates of 2 MHz s^{-1} around 20 cm wavelength, taken as evidence for a disturbance propagating “downward” in the plasma emission interpretation (Jackson et al. 1987); and c) in solar terminology, rapid broadband pulsations, “sudden (flux) reductions”, and positive and negative drift rates of $250\text{--}1000 \text{ MHz s}^{-1}$ (Bastian et al. 1990; Abada-Simon et al. 1994, 1997).

Spectral bandwidths as 1% of the emitting frequency were found for some bursts. If we conservatively assume a magnetic scale height of $L_B = 1R_*$ (assuming that the emission is gyromagnetic), the source size can be estimated to be

$$r \approx \frac{\Delta\nu}{\nu} L_B \quad (53)$$

which is \approx a few 1000 km for $L_B = R_*$ of an M dwarf, again implying very high T_b , compatible with the above light time argument (Lang & Willson 1988; Güdel et al. 1989a; Bastian et al. 1990).

Recent developments have permitted recording quite broad regions of the stellar burst spectrum, allowing for a much better characterization of the burst types. Osten & Bastian (2006) obtained burst spectra from AD Leo recorded in the 1120–1620 MHz range with a time resolution of 10 ms and a spectral resolution of 0.78 MHz. They find significant frequency-time drifts in short subbursts (Fig. 17). The main characteristics of these structures are (i) durations of about 30 ms, (ii) high polarization ($> 90\%$), frequency bandwidths of $\Delta\nu/\nu \approx 5\%$, and inverse drift rates (time interval per drift

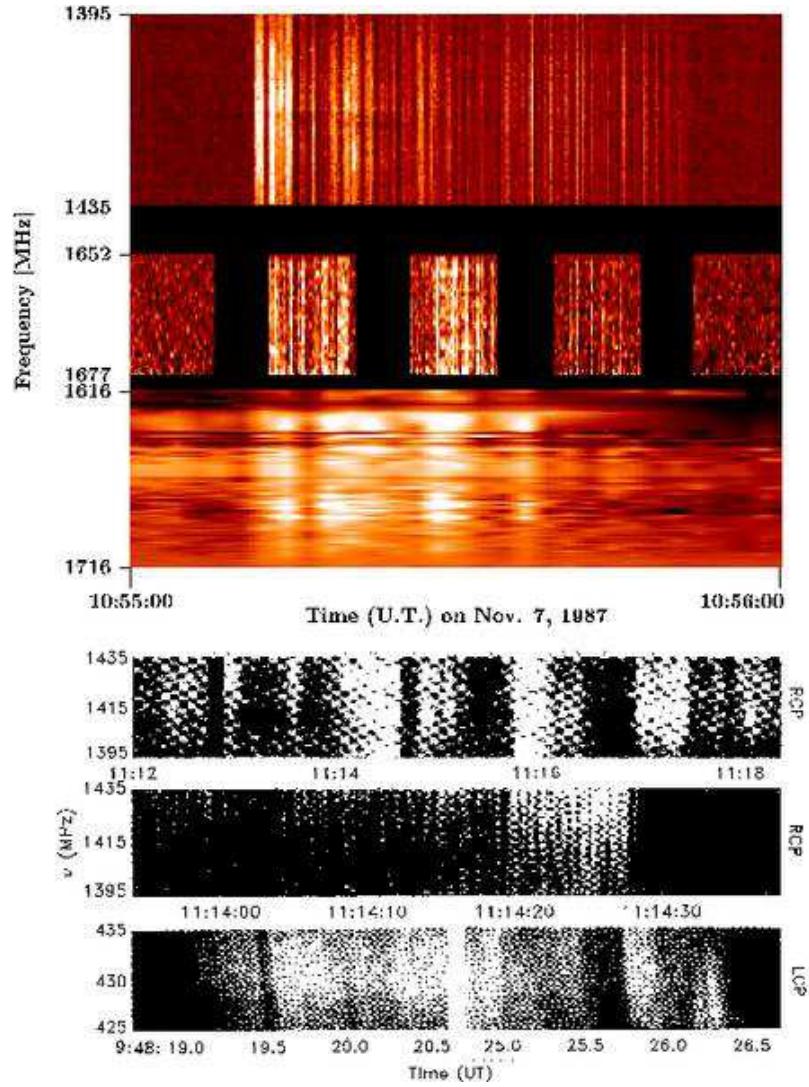


Fig. 16. Radio dynamic spectra of M dwarf flares. Upper three panels show a flare on AD Leo, recorded with the Arecibo (top), Effelsberg (middle) and Jodrell Bank (bottom) telescopes in different wavelength ranges (see also Güdel et al. 1989a). Bottom three panels show flares on AD Leo (top and middle) and YZ CMi (bottom) observed at Arecibo (after Bastian et al. 1990, reproduced with permission of the AAS).

in frequency) that are symmetric around zero, with a characteristic width corresponding to a frequency drift of 2.2 GHz s^{-1} . These characteristics are very close to those of narrow-band *solar* decimetric “spike bursts” but set

them apart from type III bursts associated with electron beams in the solar corona (type III bursts have considerably longer durations, occupy broader frequency intervals, and are at best moderately polarized).

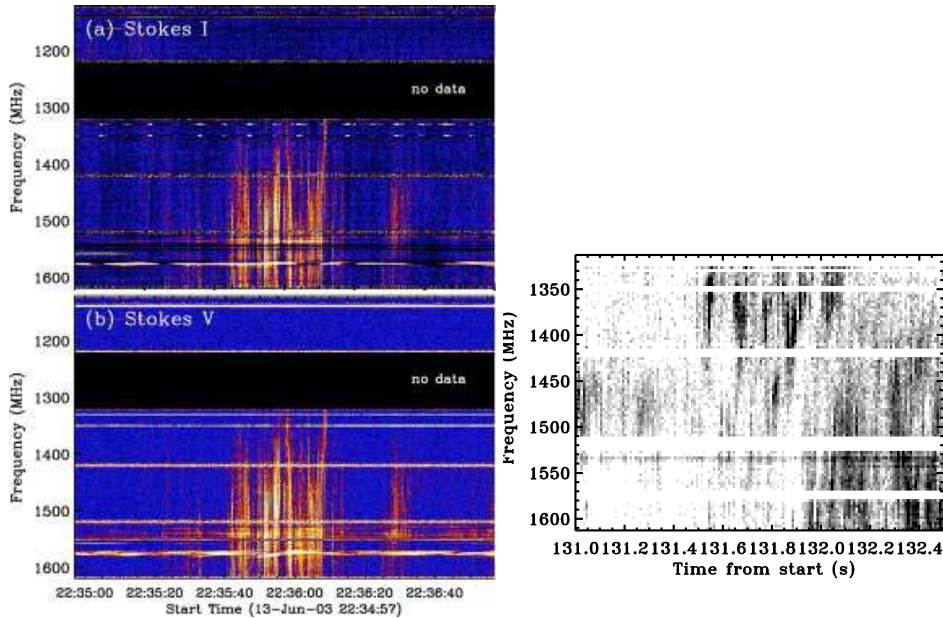


Fig. 17. Dynamic spectra of radio bursts observed in AD Leo (Osten & Bastian 2006). The left figure shows the entire event, the right figure shows an extract revealing frequency drifts and spectral structure.

There is one significant difference between the stellar and solar bursts: the duration of the solar examples is about three times shorter. We can relate this to Coulomb collisional damping (Güdel & Benz 1990; Osten & Bastian 2006) which is determined by the electron-ion collision time τ_{ei} , from which we find

$$T = 8100 \nu_{\text{MHz}}^{4/3} \tau^{2/3}. \quad (54)$$

We now identify τ with the observed characteristic event duration, and ν_{MHz} with the radio frequency in MHz. For solar events at 1.5 GHz, $T \approx 5$ MK (Güdel & Benz 1990), but for the longer events on AD Leo, $T \approx 13$ MK (Osten & Bastian 2006), which can be explained by the higher coronal temperature of AD Leo (Güdel et al. 2003a). Conversely, the higher temperature of AD Leo's corona increases the gyroresonance absorption coefficient for underlying electron cyclotron maser emission significantly:

$$\kappa_{\text{gr}} \propto T^{s-1} \quad (55)$$

where $s = 2, 3$ is the harmonic of the absorbing layer, making the escape of the preferred harmonics of the maser difficult. This is not the case for plasma

radiation for which free-free absorption is relevant:

$$\kappa_{\text{ff}} \propto T^{-3/2}, \quad (56)$$

implying that the higher temperature of AD Leo's corona clearly favors a plasma emission process as long as $\omega_p > \Omega_c$. The latter condition is easily met as it requires $B < 500$ G. This is a nice example where a stellar observation helps identify the relevant emission mechanism that remains equivocal under solar conditions.

8 Stellar X-ray flares

8.1 Cooling physics

Flares cool through radiative, conductive, and possibly also volume expansion processes. We define the flare decay phase as the episode when the net energy loss by cooling exceeds the energy gain by heating, and the total thermal energy of the flare plasma decreases. The thermal energy decay time scale τ_{th} is defined as

$$\tau_{\text{th}} = \frac{E}{\dot{E}} \quad (57)$$

where $E \approx 3n_e kT$ (for $n_e \approx n_{\text{H}}$) is the total thermal energy density in the flaring plasma of electron density n_e and temperature T , and \dot{E} is the volumetric cooling loss rate (in $\text{erg cm}^{-3} \text{s}^{-1}$). For conduction across temperature gradients in parallel magnetic fields, the mean loss rate per unit volume is

$$\dot{E}_c = \frac{1}{L} \kappa_0 T^{5/2} \frac{dT}{ds} \approx \frac{4}{7L^2} \kappa_0 T^{7/2} \quad (58)$$

where s is the coordinate along the field lines, and the term $\kappa_0 T^{5/2} dT/ds$ is the conductive flux in the approximation of Spitzer (1962), to be evaluated near the loop footpoint where T drops below 10^6 K, with $\kappa_0 \approx 9 \times 10^{-7} \text{ erg cm}^{-1} \text{s}^{-1} \text{K}^{-7/2}$. Equations (57, 58) define the *conductive time scale* $\tau_{\text{th}} \equiv \tau_c$. The second equation in (58) should be used only as an approximation for non-radiating loops with a constant cross section down to the loss region and with uniform heating (or for time-dependent cooling of a constant-pressure loop without heating; for the factor of 4/7, see Dowdy et al. 1985; Kopp & Poletto 1993). We have used L for the characteristic dimension of the source along the magnetic field lines, for example the half-length of a magnetic loop. Strictly speaking, energy is not lost by conduction but is redistributed within the source; however, we consider energy lost when it is conducted to a region that is below X-ray emitting temperatures, e.g., the transition region/chromosphere at the magnetic loop footpoints.

Radiative losses are by bremsstrahlung (dominant for $T \gtrsim 20$ MK), 2-photon continuum, bound-free, and line radiation. We note that the plasma

composition in terms of element abundances can modify the cooling function $\Lambda(T)$, but the correction is of minor importance because stellar flares are usually rather hot. At relevant temperatures, the dominant radiative losses are by bremsstrahlung, which is little sensitive to modifications of the heavy-element abundances. The energy loss rate is

$$\dot{E}_r = n_e n_H \Lambda(T) \quad (59)$$

For $T \geq 20$ MK, $\Lambda(T) = \Lambda_0 T^\gamma \approx 10^{-24.66} T^{1/4}$ erg cm³ s⁻¹ (after van den Oord & Mewe 1989 and Mewe et al. 1985). Equations (57, 59) define the *radiative time scale* $\tau_{\text{th}} \equiv \tau_r$.

8.2 Interpretation of the decay time

Equations (57), (58), and (59) describe the decay of the thermal energy, which in flare plasma is primarily due to the decay of temperature (with a time scale τ_T) and density. In contrast, the observed light curve decays (with a time scale τ_d for the *luminosity*) primarily due to the decreasing EM and, to a lesser extent, due to the decrease of $\Lambda(T)$ with decreasing temperature above ≈ 15 MK. From the energy equation, the thermal energy decay time scale τ_{th} is found to be

$$\frac{1}{\tau_{\text{th}}} = \left(1 - \frac{\gamma}{2}\right) \frac{1}{\tau_T} + \frac{1}{2\tau_d} \quad (60)$$

where the right-hand side is usually known from the observations (see van den Oord et al. 1988 for a derivation). The decay time scale of the EM then follows as $1/\tau_{\text{EM}} = 1/\tau_d - \gamma/\tau_T$. Pan et al. (1997) derived somewhat different coefficients in (60) for the assumption of constant volume or constant mass, including the enthalpy flux. In the absence of measurements of τ_T , it is often assumed that $\tau_{\text{th}} = \tau_d$ although this is an inaccurate approximation.

In (60), τ_{th} is usually set to be τ_r or τ_c or, if both loss terms are significant, $(\tau_r^{-1} + \tau_c^{-1})^{-1}$, taken at the beginning of the flare decay (note again that a simple identification of τ_r with τ_d is not accurate). If radiative losses dominate, the density immediately follows from (57, 59)

$$\tau_{\text{th}} \approx \frac{3kT}{n_e \Lambda(T)} \quad (61)$$

and the characteristic size scale ℓ of the flaring plasma or the flare-loop semi-length L for a sample of \mathcal{N} identical loops follow from

$$\text{EM} = n_e n_H (\Gamma + 1) \pi \alpha^2 \mathcal{N} L^3 \approx n^2 \ell^3 \quad (62)$$

where α is the loop aspect ratio (ratio between loop cross sectional diameter at the base and total length $2L$) and Γ is the loop expansion factor. The

loop height for the important case of dominant radiative losses follows to be (White et al. 1986; van den Oord et al. 1988)

$$H = \left(\frac{8}{9\pi^4} \frac{A_0^2}{k^2} \right)^{1/3} \left(\frac{\text{EM}}{T^{3/2} \tau_r^2} \right)^{1/3} (\mathcal{N}\alpha^2)^{-1/3} (\Gamma + 1)^{-1/3}. \quad (63)$$

A lower limit to H is found for $\tau_r \approx \tau_c$ in the same treatment:

$$H_{\min} = \frac{A_0}{\kappa_0 \pi^2} \frac{\text{EM}}{T^{3.25}} (\mathcal{N}\alpha^2)^{-1}. \quad (64)$$

\mathcal{N} , α , and Γ are usually unknown and treated as free parameters within reasonable bounds. Generally, a small \mathcal{N} is compatible with dominant radiative cooling.

8.3 Quasi-static cooling loops

van den Oord & Mewe (1989) derived the energy equation of a cooling magnetic loop in such a way that it is formally identical to a static loop (Rosner et al. 1978), by introducing a slowly varying flare heating rate that balances the total energy loss, and a possible constant heating rate during the flare decay. This specific solution thus proceeds through a sequence of different (quasi-)static loops with decreasing temperature.

The general treatment involves continued heating that keeps the cooling loop at coronal temperatures. If this constant heating term is zero, one finds for free quasi-static cooling

$$T(t) = T_0(1 + t/3\tau_{r,0})^{-8/7} \quad (65)$$

$$L_r(t) = L_{r,0}(1 + t/3\tau_{r,0})^{-4} \quad (66)$$

$$n_e(t) = n_{e,0}(1 + t/3\tau_{r,0})^{-13/7} \quad (67)$$

where L_r is the total radiative loss rate, and $\tau_{r,0}$ is the radiative loss time scale (61) at the beginning of the flare decay.

This prescription is equivalent to requiring a constant ratio between radiative and conductive loss times, i.e., in the approximation of $T \gtrsim 20$ MK ($\Lambda \propto T^{1/4}$)

$$\frac{\tau_r}{\tau_c} = \text{const} \frac{T^{13/4}}{\text{EM}} \approx 0.18. \quad (68)$$

Accordingly, the applicability of the quasi-static cooling approach can be supported or rejected based on the run of T and EM during the decay phase. Note, however, that a constant ratio (68) is not a sufficient condition to fully justify this approach.

8.4 Cooling loops with continued heating

Whether or not flaring loops indeed follow a quasi-static cooling path is best studied on a density-temperature diagram (Fig. 18). Usually, characteristic values $T = T_a$ and $n_e = n_{e,a}$ as measured at the loop apex are used as diagnostics. For a magnetic loop in hydrostatic equilibrium, with constant cross section assumed, the RTV scaling law (33) requires stable solutions (T, n_e) to be located where $T^2 \approx 7.6 \times 10^{-7} n_e L$ (for $n_e = n_i$). On a diagram of $\log T$ vs. $\log n_e$, all solutions are therefore located on a straight line with slope $\zeta = 0.5$. Figure 18 shows the path of a hydrodynamically simulated flare. The initial rapid heating leads to a rapid increase of T , inducing increased losses by conduction. As chromospheric evaporation grows, radiation helps to balance the heating energy input. The flare decay sets in once the heating rate drops. At this moment, depending on the amount of ongoing heating, the magnetic loop is too dense to be in equilibrium, and the radiative losses exceed the heating rate, resulting in a thermal instability. In the limit of no heating during the decay, that is, an abrupt turn-off of the heating at the flare peak, the slope of the path becomes

$$\zeta \equiv \frac{d \ln T}{d \ln n_e} \equiv \frac{\tau_n}{\tau_T} = 2 \quad (69)$$

implying $T(t) \propto n_e^\zeta(t) = n_e^2(t)$ (see Serio et al. 1991 for further discussion). Here, τ_T and τ_n are the e-folding decay times of the temperature and the electron density, respectively, under the assumption of exponential decay laws. Only for a non-vanishing heating rate does the loop slowly recover and eventually settle on a new equilibrium locus (Fig. 18). In contrast, if heating continues and is very gradually reduced, the loop decays along the static solutions ($\zeta = 0.5$). Observationally, this path is often followed by large solar flares (Jakimiec et al. 1992).

Applying this concept to stellar astronomy, we replace n_e by the observable \sqrt{EM} and thus assume a constant flare volume, and further introduce the following generalization. In the freely cooling case after an abrupt heating turnoff, the entropy per particle at the loop apex decays on the thermodynamic decay time

$$\tau_{td} = 3.7 \times 10^{-4} \frac{L}{T_0^{1/2}} \quad [\text{s}] \quad (70)$$

where T_0 is the flare temperature at the beginning of the decay (Serio et al. 1991). When heating is present, we introduce a correction term $F(\zeta) \equiv \tau_{LC}/\tau_{td}$ (Reale et al. 1997; τ_{LC} is the observed light curve decay time)

$$\tau_{LC} = 3.7 \times 10^{-4} \frac{L}{T_0^{1/2}} F(\zeta) \quad [\text{s}] \quad (71)$$

$F(\zeta)$ is therefore to be numerically calibrated for each X-ray telescope. With known F , (71) can be solved for L . This scheme thus offers i) an indirect

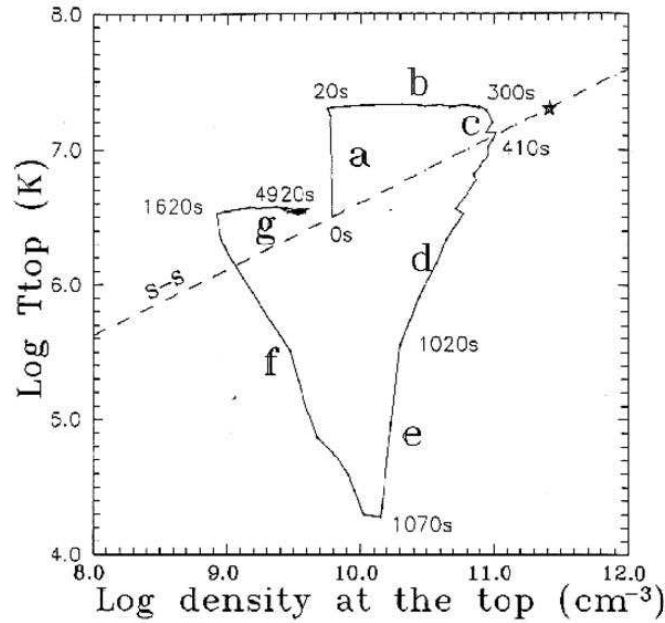


Fig. 18. Density-temperature diagram of a hydrodynamically simulated flare. The flare loop starts from an equilibrium (S-S, steady-state loop according to Rosner et al. 1978); (a) and (b) refer to the heating phase; at (c), the heating is abruptly turned off, after which the loop cools rapidly (d, e), and only slowly recovers toward a new equilibrium solution (f, g) due to constant background heating (from Jakimiec et al. 1992).

method to study flaring loop geometries (L), ii) a way of determining the rate and decay time scale of continued heating via $F(\zeta)$ and τ_{td} , and iii) implications for the density decay time via $\tau_n = \zeta\tau_T$. Conditions of applicability include $\zeta \geq 0.3$ (most values are found in the range of $\sim 0.3 - 1$, Reale et al. 1997) and a resulting loop length L of less than one pressure scale height.

8.5 Two-Ribbon flare models

An approach that is entirely based on continuous heating (as opposed to cooling) was developed for the two-ribbon (2-R) class of solar flares. An example of this flare type is shown in Fig. 19. The 2-R flare model devised initially by Kopp & Poletto (1984) is a parameterized magnetic-energy release model. The time development of the flare light-curve is completely determined by the amount of energy available in non-potential magnetic fields, and by the rate of energy release as a function of time and geometry as the fields reconnect and relax to a potential-field configuration. It is assumed that a portion of the total energy is radiated into the observed X-ray band, while the remaining

energy will be lost by other mechanisms. 2-R flares are well established for the Sun (Fig. 19); they often lead to large, long-duration flares that may be accompanied by mass ejections.

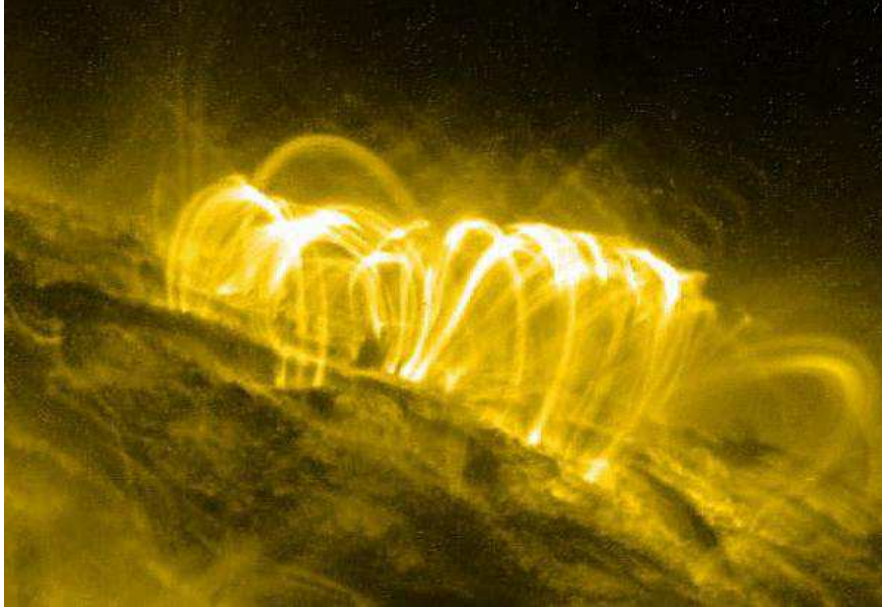


Fig. 19. Trace image of a flaring magnetic loop arcade.

The magnetic fields are, for convenience, described along meridional planes on the star by Legendre polynomials P_n of order n , up to the height of the neutral point; above this level, the field is directed radially, that is, the field lines are “open”. As time proceeds, field lines nearest to the neutral line move inward at coronal levels and reconnect at progressively larger heights above the neutral line. The reconnection point thus moves upward as the flare proceeds, leaving closed magnetic-loop systems underneath. One loop arcade thus corresponds to one N-S aligned lobe between two zeros of P_n in latitude, axisymmetrically continued over some longitude in E-W direction. The propagation of the neutral point in height, $y(t)$, with a time constant t_0 , is prescribed by (y in units of R_* , measured from the star’s center)

$$y(t) = 1 + \frac{H_m}{R_*} \left(1 - e^{-t/t_0}\right) \quad (72)$$

$$H(t) \equiv [y(t) - 1]R_* \quad (73)$$

and the total energy release of the reconnecting arcade per radian in longitude is equal to the magnetic energy lost by reconnection,

$$\frac{dE}{dy} = \frac{1}{8\pi} 2n(n+1)(2n+1)^2 R_*^3 B^2 I_{12}(n) \frac{y^{2n}(y^{2n+1}-1)}{[n+(n+1)y^{2n+1}]^3} \quad (74)$$

$$\frac{dE}{dt} = \frac{dE}{dy} \frac{dy}{dt} \quad (75)$$

(Poletto et al. 1988). In (72), H_m is the maximum height of the neutral point for $t \rightarrow \infty$; typically, H_m is assumed to be equal to the latitudinal extent of the loops, i.e.,

$$H_m \approx \frac{\pi}{n+1/2} R_* \quad (76)$$

for $n > 2$ and $H_m = (\pi/2)R_*$ for $n = 2$. Here, B is the surface magnetic field strength at the axis of symmetry, and R_* is the stellar radius. Finally, $I_{12}(n)$ corresponds to $\int [P_n(\cos\theta)]^2 d(\cos\theta)$ evaluated between the latitudinal borders of the lobe (zeros of $dP_n/d\theta$), and θ is the co-latitude.

The free parameters are B and the efficiency of the energy-to-radiation conversion, q , both of which determine the normalization of the light curve; the time scale of the reconnection process, t_0 , and the polynomial degree n determine the duration of the flare; and the geometry of the flare is fixed by n and therefore the asymptotic height H_m of the reconnection point. The largest realistic 2-R flare model is based on the Legendre polynomial of degree $n = 2$; the loop arcade then stretches out between the equator and the stellar poles. Usually, solutions can be found for many larger n as well. However, because a larger n requires larger surface magnetic field strengths, a natural limit is set to n within the framework of this model. Once the model solution has been established, further parameters, in particular the electron density n_e , can be inferred.

8.6 A magnetohydrodynamic model

Some scaling laws have been obtained from simulations based on the full set of magnetohydrodynamic equations (Shibata & Yokoyama 1999, 2002). For the flare peak temperature T , the loop magnetic field strength B , the pre-flare loop electron density n_0 , and the loop semi-length L , one finds, under the condition of dominant conductive cooling (appropriate for the early phase of a flare),

$$T \approx 1.8 \times 10^4 B^{6/7} n_0^{-1/7} L^{2/7} \text{ [K]}. \quad (77)$$

The law follows from the balance between conduction cooling ($\propto T^{7/2}/L^2$, 58) and magnetic reconnection heating ($\propto B^3/L$). Assuming loop filling through chromospheric evaporation and balance between thermal and magnetic pressure in the loop, two further ‘‘pressure-balance scaling laws’’ follow:

$$EM \approx 3 \times 10^{-17} B^{-5} n_0^{3/2} T^{17/2} \text{ [cm}^{-3}\text{]} \quad (78)$$

$$EM \approx 2 \times 10^8 L^{5/3} n_0^{2/3} T^{8/3} \text{ [cm}^{-3}\text{]}. \quad (79)$$

An alternative scaling law applies if the density development in the initial flare phase is assumed to follow balance between evaporation enthalpy-flux and conduction flux, although the observational support is weaker,

$$\text{EM} \approx 1 \times 10^{-5} B^{-3} n_0^{1/2} T^{15/2} [\text{cm}^{-3}]. \quad (80)$$

And third, a steady solution is found for which the radiative losses balance conductive losses. This scaling law applies to a steady loop,

$$\text{EM} \approx \begin{cases} 10^{13} T^4 L & [\text{cm}^{-3}] & \text{for } T < 10^7 \text{ K} \\ 10^{20} T^3 L & [\text{cm}^{-3}] & \text{for } T > 10^7 \text{ K} \end{cases} \quad (81)$$

and is equivalent to the RTV scaling law (33).

The advantage of these scaling laws is that they make use exclusively of the flare-peak parameters T , EM , B (and the pre-flare density n_0) and do not require knowledge of the time evolution of these parameters.

8.7 Observations of stellar X-ray flares

One of the main results that have come from extensive modeling of stellar X-ray flares is that extremely large stellar flares require large volumes under all realistic assumptions for the flare density, i.e., flaring complexes of magnetic loops must either be high, or must spread across a large surface area. This is because, first, the energy derives from the non-potential portion of the magnetic fields that are probably no stronger than a few 100 G in the corona; and second, small-loop models require higher pressure to produce the observed luminosity, hence requiring excessively strong magnetic fields.

There is extensive literature discussing individual flares observed on a variety of stars. I will not discuss these results individually here. The interested reader may consult the compilation of results in Güdel (2004) and the references given therein. This section summarizes some systematic trends found in stellar flares.

When the flare energy release evaporates plasma into the corona, heating and cooling effects compete simultaneously, depending on the density and temperature profiles in a given flare. It is therefore quite surprising to find a broad correlation between peak temperature T_p and peak emission measure EM_p , as illustrated in Fig. 20 for the sample reported in Güdel (2004). A regression fit gives (for 66 entries)

$$\text{EM}_p \propto T_p^{4.30 \pm 0.35}. \quad (82)$$

The correlation overall indicates that *larger flares are hotter*. A similar relation was reported previously for solar flares (Feldman et al. 1995).

It is interesting to note that this correlation is similar to the $T - L_X$ correlation for the “non-flaring” coronal stars in Fig. 7 at cooler temperatures. This same sample is plotted as triangles in Fig. 20, again only for the hotter

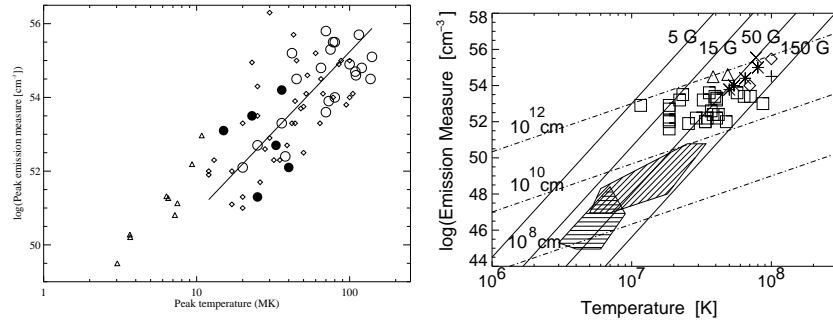


Fig. 20. *Left:* Peak temperatures and EMs of the flares (from Güdel 2004 and references therein). Key to the symbols: Filled circles: *XMM-Newton* observations. Open circles: *ASCA* or *BeppoSAX* observations. Small diamonds: observations from other satellites. The solid line shows a regression fit (82). Triangles represent non-flaring parameters of G stars, referring to the hotter plasma component in 2-*T* spectral fits to *ROSAT* data. – *Right:* Theoretical EM-*T* relations based on the reconnection model by Shibata & Yokoyama, showing lines of constant loop length *L* and lines of constant magnetic field strength *B*. Hatched areas are loci reported for solar flares, and other symbols refer to individual stellar flares in star-forming regions (figure courtesy of K. Shibata and T. Yokoyama, after Shibata & Yokoyama 2002).

plasma component. The stars follow approximately the same slope as the flares, albeit at cooler temperatures, and for a given temperature, the EM is higher. This trend may suggest that flares systematically contribute to the hot plasma component, although we have not temporally averaged the flare temperature and EM for this simple comparison.

In the context of the magnetohydrodynamic scaling laws presented in (77)–(78), the observed loci of the flares require loop magnetic field strengths similar to solar flare values ($B \approx 10 - 150$ G) but the loop lengths must increase toward larger flares. This is seen in Fig. 20 where lines of constant *L* and *B* are plotted for this flare model. Typical loop lengths are thus of order $L \approx 10^{11}$ cm in this interpretation.

8.8 The “Neupert Effect”

In the framework of chromospheric evaporation, we assume that the emitted radio emission or its flux at Earth, $F_R(t)$ is at any time proportional to the deposition rate of kinetic energy by nonthermal electrons into the plasma of the chromosphere. This plasma is thereby heated and “evaporates” into the corona. We define the conversion factor α as the ratio between the *thermal* energy flux being deposited in the chromosphere by nonthermal electrons and the observed radio flux density. Conversion into other forms of energy (mechanical, turbulence, etc.) occurs in parallel. Our simplification consists,

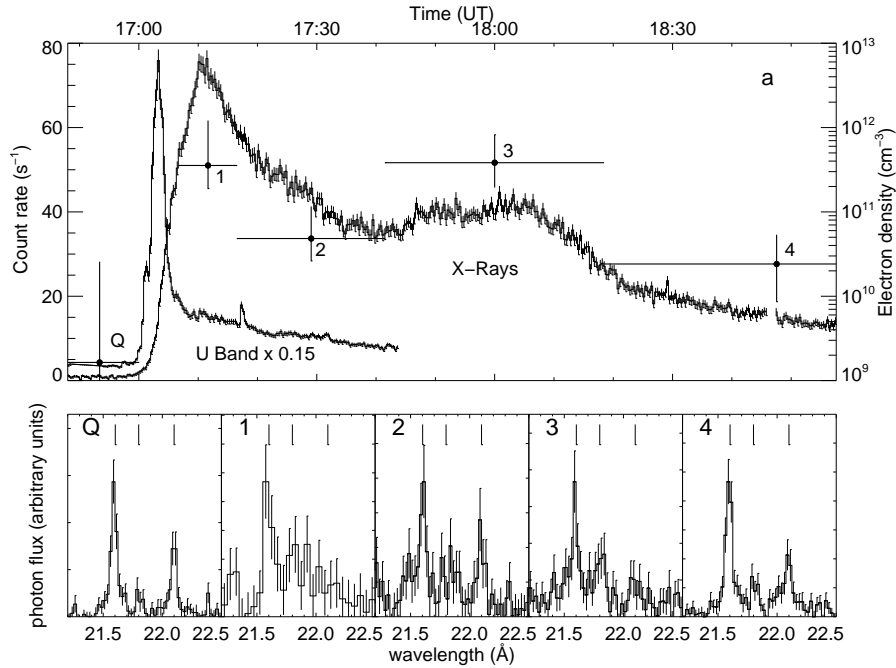


Fig. 21. Flare on Proxima Centauri, observed with *XMM-Newton*. The top panel shows the X-ray light curve and the much shorter U band flare (around 17 UT). The bottom panel shows the O VII He-like triplets observed during various time intervals of the flare. The locations of the *r*, *i*, and *f* lines are marked by vertical lines. The resulting electron densities are given in the top panel by the crosses, where the horizontal arm lengths indicate the time intervals over which the data were integrated, and the right axis gives the logarithmic scale (after Güdel et al. 2002a).

first, in the assumption that these other energy transformations do not interact so that α remains constant over the course of the relatively short radio flare; second, we will assume that the dominant losses of the *thermal* energy occur via radiation; we will neglect energy loss into cool, non-X-ray emitting plasma, e.g. by conduction, and cooling by adiabatic expansion. Also, we assume that there is no direct heating in parallel to the chromospheric evaporation. Third, we will use one temperature parameter for the flare plasma at any given time: The temperature T can be considered as describing an isothermal plasma dominating the total losses from the flaring loops.

The rate of change of the total thermal energy E in a plasma of volume V with electron density n_e is determined by the influx of kinetic energy and by radiation, hence the energy conservation equation for the *thermal* plasma is

$$\frac{d}{dt}(3n_e kTV) = \alpha F_R(t) - n_e^2 V \Lambda(T) \quad (83)$$

where $\Lambda(T)$ is the total luminosity of a plasma with unit emission measure (EM) at a temperature of T . Note again that (83) does, by definition of α , not describe the total energy budget of the flare, but merely the energy conversion of interest here. For large flare temperatures ($\gg 20$ MK), Λ is dominated by bremsstrahlung losses, roughly scaling as $T^{1/2}$. For somewhat more moderate temperatures ($\gtrsim 10 - 20$ MK), losses via line emission become important, with the (isothermal) approximation for Λ

$$\Lambda(T) = 1.86 \cdot 10^{-25} T^{1/4} \text{ [erg s}^{-1} \text{ cm}^3\text{]} \quad (84)$$

(see after equation 59 - for simplicity, we define here $\text{EM} = n_e^2 V$ with $n_H = 0.85n_e$ and a corresponding correction in Λ). In the absence of kinetic energy influx $\alpha F_R(t)$, the thermal energy decays radiatively (neglecting conduction), and hence we define an e-folding decay time τ for the thermal energy as a function of the two independent variables temperature T and density n_e at a given instant,

$$\left. \frac{dE(t)}{dt} \right|_{F_R=0} = \frac{E(t)}{\tau(n_e(t), T(t))} \quad (85)$$

so that

$$\tau(n_e(t), T(t)) = \frac{E(t)}{L_{\text{rad}}(t)} = \frac{3kT}{n_e \Lambda(T)} \quad (86)$$

where L_{rad} is the total luminosity (approximately = X-ray luminosity, L_X , but also contributions from lower temperatures, e.g., in the ultraviolet, which we neglect here). Then,

$$\frac{dE(t)}{dt} = \alpha F_R(t) - L_{\text{rad}}(t) = \alpha F_R(t) - \frac{E(t)}{\tau(t)}. \quad (87)$$

The general solution of the inhomogeneous, linear differential equation (87) reads

$$E(t) = e^{-\int_{t_0}^t \tau(y)^{-1} dy} \left(E_0 + \alpha \int_{t_0}^t F_R(u) e^{+\int_{t_0}^u \tau(y)^{-1} dy} du \right) \quad (88)$$

where $E_0 = E(t_0)$ for a fixed t_0 before the flare start. The integration over τ^{-1} is along the time axis. If the initial thermal energy content can be neglected ($E_0 = 0$), then

$$E(t) = \alpha \int_{t_0}^t F_R(u) e^{-\int_u^t \tau(y)^{-1} dy} du. \quad (89)$$

We define an average decay constant for any time interval $[u, t]$ by

$$\bar{\tau}^{-1} = \bar{\tau}^{-1}(u, t) = \frac{\int_u^t \tau(y)^{-1} dy}{t - u}. \quad (90)$$

Then

$$E(t) = \alpha \int_{t_0}^t F_{\text{R}}(u) e^{-(t-u)/\bar{\tau}(t,u)} du, \quad (91)$$

i.e., for constant τ the energy profile is the *convolution* of the kinetic energy influx with an exponential function. Equation (91) is a generalized form of the *Neupert effect*. In the limit $\tau \rightarrow \infty$, (87) and (91) become

$$\frac{dE(t)}{dt} = \alpha F_{\text{R}}(t) \quad (92)$$

$$E(t) = \alpha \int_{t_0}^t F_{\text{R}}(u) du, \quad (93)$$

i.e., the total energy content of the plasma is the integral of the kinetic energy influx (and radiation is inhibited). Equations (92) and (93) remind us of the classical formulation of the Neupert effect, with the observed X-ray losses replaced by the thermal energy content of the plasma. These two equations are applicable only for the increasing portion of the soft X-ray light curve or, correspondingly, for the time interval where $F_{\text{R}} \neq 0$. On using (86), we obtain the generalized Neupert effect for the light curve,

$$L_{\text{rad}}(t) = \frac{\alpha}{\tau(t)} \int_{t_0}^t F_{\text{R}}(u) e^{-(t-u)/\bar{\tau}(t,u)} du. \quad (94)$$

Note the importance of the thermal *energy* decay time $\tau = 3kT/(n_e\Lambda(T))$. Serio et al. (1991) and Jakimiec et al. (1992) find $Tn^{-2} = \text{const}$ for the radiative cooling phase. If the temperatures are very high and the bremsstrahlung approximation applies, then $\tau = T^{1/2}n^{-1}$ and thus $\tau = \text{const}$ in (94). However, in the case of more moderate temperatures (84), only for $T^{3/4}n^{-1} = \text{const}$ does the classical Neupert effect approximately apply to the light curve. The actual functional dependence of $\psi(T)$ is more complicated. Thus, in general, the relevant parameters to be investigated for the Neupert effect are the *energies*. Further, $L_{\text{rad}}(t)$ describes all radiative losses across the electromagnetic spectrum; the observed X-ray luminosity L_{X} generally depends on the selected bandpass and therefore constitutes only a lower limit to L_{rad} .

Despite these caveats, it is surprising that the Neupert effect is often well seen, at least qualitatively, in solar radio and X-ray light curves. Instead of radio emission, bursts can be monitored in the U band: because they are likely to be a prompt reaction to the bombardment of the chromosphere by the same electron population that induces gyrosynchrotron emission, the Neupert effect should hold as well. A stellar example is shown in Fig. 21. These observations give clear evidence that at least some giant flares on active stars are subject to similar evaporation physics as known from the solar corona.

9 The statistics of flares

The study of coronal structure confronts us with several problems that are difficult to explain by scaling of solar coronal structure: i) Characteristic coronal temperatures increase with increasing magnetic activity. ii) Characteristic coronal densities are typically higher in active than in inactive stars, and pressures in hot loops can be exceedingly high. iii) The maximum stellar X-ray luminosities exceed the levels expected from complete coverage of the surface with solar-like active regions by up to an order of magnitude. iv) Radio observations reveal a persistent population of non-thermal high-energy electrons in magnetically active stars even if the lifetime of such a population should only be tens of minutes to about an hour under ideal trapping conditions in coronal loops and perhaps much less due to efficient scattering of electrons into the chromosphere. Several of these features are reminiscent of flaring, as are some structural elements in stellar coronae. If flares are important for any of the above stellar coronal properties indeed, then we must consider the effects of frequent flares that may be unresolved in our observations but that may make up part, if not all, of the “quiescent” emission.

9.1 Stochastic variability - what is “quiescent emission”?

The problem has been attacked in several dedicated statistical studies. Early statistical investigations (fluctuation analysis in light curves) remained ambiguous, reporting a significant amount of variability, although not necessarily being due to flares, or statistical absence of low-level flaring within the sensitivity limits (e.g., Ambruster et al. 1987; Collura et al. 1988; Pallavicini et al. 1990). There are indications in newer data that M dwarfs are continuously variable on short ($\lesssim 1$ day) time scales, and that the luminosity distribution is very similar to the equivalent distribution derived for solar flares, which suggests that the overall stellar light curves of dM stars are variable in the same way as a statistical sample of solar flares (Marino et al. 2000).

Very long light curves obtained from the *EUVE* satellite reveal an astonishing level of continuous variability in active M dwarfs. Some of those data can be used to investigate statistical properties of the occurrence rate of flares as a function of total emitted energy. The increased sensitivity of *XMM-Newton* and *Chandra* is now revealing extreme levels of activity. Some X-ray light curves show no steady time interval exceeding a few tens of minutes within the sensitivity limit. In the day-long light curve in Fig. 23, no more than 30%, and probably much less, of the average X-ray emission of UV Cet can be attributed to any sort of steady emission, even outside the obvious, large flares. On the contrary, almost the entire light curve is resolved into frequent, stochastically occurring flares of various amplitudes.

In the *solar* corona, the flare rate increases steeply toward lower radiative energies, with no evidence (yet) for a lower threshold (e.g., Krucker & Benz 1998). Figure 24 shows an example of a *GOES* light curve in the 1.5-12 keV

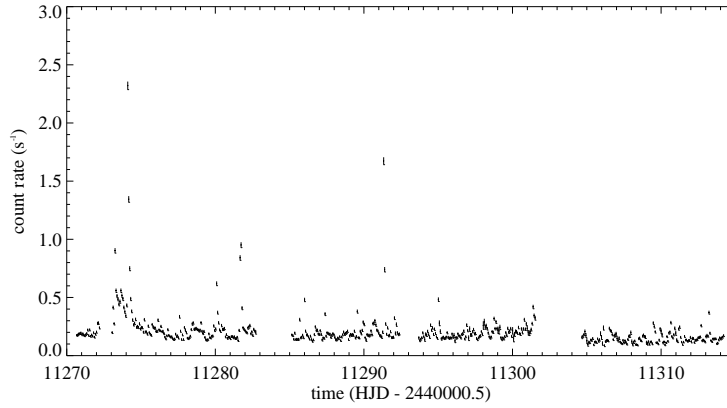


Fig. 22. A long light curve of the dMe star AD Leo, obtained by the DS instrument on *EUVIE*. Most of the discernible variability is due to flares (after Güdel et al. 2003a).

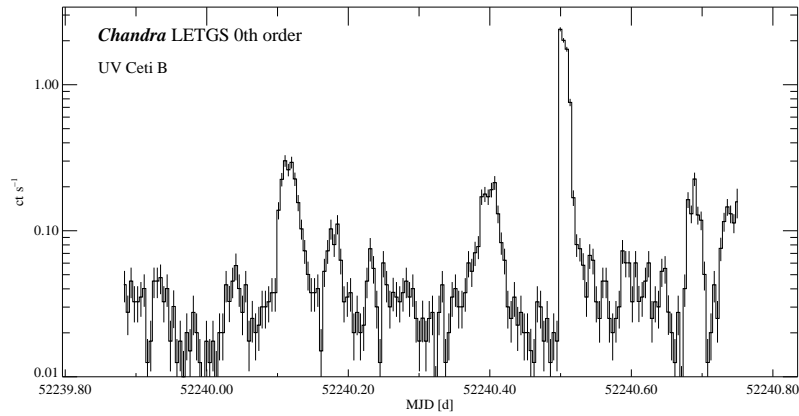


Fig. 23. Light curve of UV Ceti B, observed with the *Chandra* LETGS/HRC during about 1 day. Note the logarithmic flux axis (figure courtesy of M. Audard, after Audard et al. 2003).

range, purposely selected during an extremely active period in November 2003. While the *GOES* band is harder than typical bands used for stellar observations, it more clearly reveals the level of the underlying variability (a typical detector used for stellar observations would see much less contrast). If the solar analogy has any merit in interpreting stellar coronal X-rays, then low-level emission in stars that do show flares *cannot* be truly quiescent, that is, constant or slowly varying exclusively due to long-term evolution of active

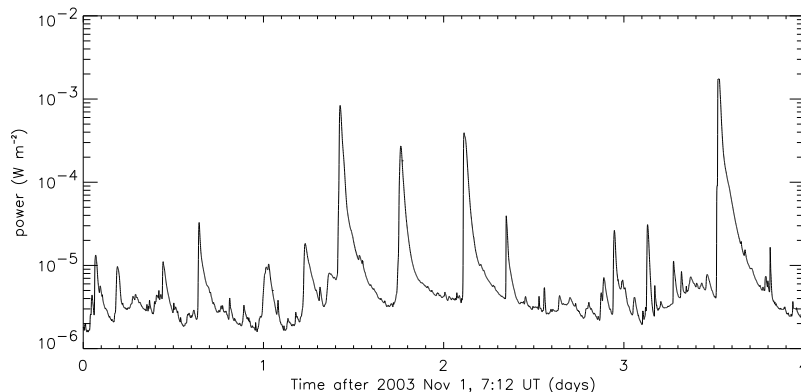


Fig. 24. *GOES* full-disk solar X-ray light curve, observed in the 1.5–12 keV band in November 2003. The abscissa gives time after 2003 November 1, 7:12 UT in days.

regions, or due to rotational modulation. A measure of *flare rates* is therefore not meaningful unless it refers to flares above a given luminosity or energy threshold. This is - emphatically - not to say that steady emission is absent in magnetically active stars. However, once we accept the solar analogy as a working principle, the question is not so much about the presence of large numbers of flares, but to what extent they contribute to the overall X-ray emission from coronae.

9.2 The flare-energy distribution

The suggestion that stochastically occurring flares may be largely responsible for coronal heating is known as the “microflare” or “nanoflare” hypothesis in solar physics (Parker 1988). Observationally, it is supported by evidence for the presence of numerous small-scale flare events occurring in the solar corona at any time (e.g., Lin et al. 1984). Their distribution in energy is a power law,

$$\frac{dN}{dE} = kE^{-\alpha} \quad (95)$$

where dN is the number of flares per unit time with a total energy in the interval $[E, E+dE]$, and k is a constant. If $\alpha \geq 2$, then the energy integration (for a given time interval) diverges for $E_{\min} \rightarrow 0$, that is, by extrapolating the power law to sufficiently small flare energies, *any* energy release power can be attained. This is not the case for $\alpha < 2$. Solar studies have repeatedly resulted in α values of 1.6–1.8 for ordinary solar flares (Crosby et al. 1993), but some recent studies of low-level flaring suggest $\alpha = 2.0$ –2.6 (Krucker & Benz 1998; Parnell & Jupp 2000).

Relevant stellar studies have been rare (see Table 3). Early investigations lumped several stars together to produce meaningful statistics. Full forward

modeling of a superposition of stochastic flares was applied to EUV and X-ray light curves by Kashyap et al. (2002) and Güdel et al. (2003a) based on Monte Carlo simulations, and by Arzner & Güdel (2004) based on an analytical formulation. The results of these investigations are in full agreement, converging to $\alpha \approx 2.0 - 2.5$ for M dwarfs (Table 3). If the power-law flare energy distribution extends by about 1–2 orders of magnitude below the actual detection limit in the light curves, then the *entire* emission could be explained by stochastic flares. The coronal heating process in magnetically active stars would - in this extreme limit - be one solely due to *time-dependent* heating by flares, or, in other words, the X-ray corona would be an entirely hydrodynamic phenomenon rather than an ensemble of hydrostatic loops.

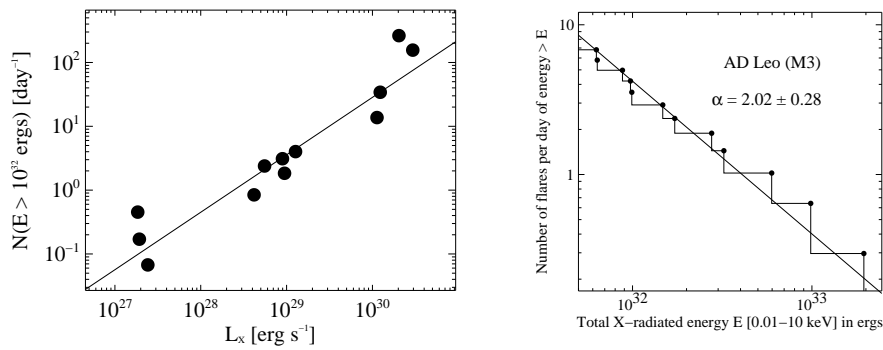


Fig. 25. *Left:* The rate of flares above a threshold of 10^{32} erg in total radiated X-ray energy is plotted against the low-level luminosity for several stars, together with a regression fit. *Right:* Flare energy distribution for AD Leo, using a flare identification algorithm for an observation with *EUVE* (both figures courtesy of M. Audard, after Audard et al. 2000).

Table 3. Stellar radiative flare-energy distributions

Star sample	Photon energies [keV]	log (Flare energies)	α	References
M dwarfs	0.05–2	30.6 – 33.2	1.52 ± 0.08	Collura et al. (1988)
M dwarfs	0.05–2	30.5 – 34.0	1.7 ± 0.1	Pallavicini et al. (1990)
RS CVn binaries	EUV	32.9 – 34.6	1.6	Osten & Brown (1999)
Two G dwarfs	EUV	33.5 – 34.8	2.0–2.2	Audard et al. (1999)
F-M dwarfs	EUV	30.6 – 35.0	1.8–2.3	Audard et al. (2000)
Three M dwarfs	EUV	29.0 – 33.7	2.2–2.7	Kashyap et al. (2002)
AD Leo	EUV&0.1–10	31.1 – 33.7	2.0–2.5	Güdel et al. (2003a)
AD Leo	EUV	31.1 – 33.7	2.3 ± 0.1	Arzner & Güdel (2004)

^aTotal flare-radiated X-ray energies used for the analysis (in ergs).

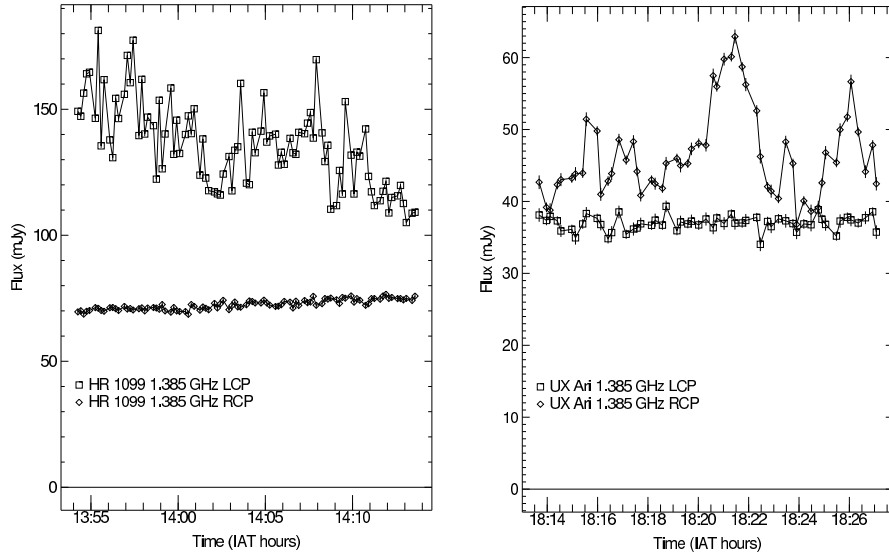


Fig. 26. Light curves of HR 1099 (*left*) and UX Ari (*right*) obtained in the two senses of circular polarization. The brighter of the two polarized fluxes varies rapidly and has been interpreted as 100% polarized coherent emission superimposed on a gradually changing gyrosynchrotron component (White & Franciosini 1995; figures from S. M. White).

9.3 Microflaring at radio wavelengths

Quiescent radio emission can apparently persist for quite long periods. Losses by collisions (11) require a very low ambient electron density to maintain the electron population. Alternatively, electrons could be frequently injected at many coronal sites. Based on spectral observations, White & Franciosini (1995) suggest that the emission around 1.4 GHz shown in Fig. 26 is composed of a steady, weakly polarized broad-band gyrosynchrotron component plus superimposed, strongly and oppositely polarized, fluctuating plasma emission that is perceived as quasi-steady but that may occasionally evolve into strong, polarized flare emission. Continual flaring may thus also reflect in radio light curves.

10 A flare-heating approach

The quiescent emission of synchrotron radiation requires the continuous presence of nonthermal electrons, while X-rays are emitted by the thermal bulk of typically 10^6 to a few times 10^7 K. For optically thin radio emission ($\nu \gtrsim 5$ GHz), the radio luminosity is

$$L_R = 4\pi\eta_\nu V_R [\text{erg s}^{-1} \text{ Hz}^{-1}], \quad (96)$$

where V_R is the radio source volume. The density of nonthermal electrons will be assumed to be distributed in energy according to a power law,

$$n(\varepsilon) = \frac{(\delta - 1)}{\varepsilon_0} N \left(\frac{\varepsilon}{\varepsilon_0} \right)^{-\delta} \quad [\text{cm}^{-3} \text{ erg}^{-1}]. \quad (97)$$

lower cutoff at $\varepsilon_0 \approx 10 \text{ keV} = 1.6 \cdot 10^{-8} \text{ erg}$ is compatible with most acceleration processes proposed for stellar coronae and with solar flare observations. We keep ε_0 fixed at 10 keV in the following considerations. It is not a sensitive value for synchrotron emission since the latter becomes appreciable only at higher energies. We assume a homogeneous source for simplicity. The gyrosynchrotron emissivity is approximately given by Dulk (1985) (sum of x and o mode, see equation 46)

$$\eta \approx 1.8 \cdot 3.3 \times 10^{-24} BN 10^{-0.52\delta} (\sin \theta)^{-0.43+0.65\delta} \left(\frac{\nu}{\nu_B} \right)^{1.22-0.90\delta} \quad (98)$$

$$\equiv 1.8 \cdot \vartheta(B, \delta, \nu, \theta) N \quad [\text{erg s}^{-1} \text{ Hz}^{-1} \text{ cm}^{-3} \text{ sterad}^{-1}], \quad (99)$$

where ν_B is the electron gyrofrequency and θ is the angle between the line of sight and the magnetic field. In a steady-state situation, the density of nonthermal electrons is given by

$$n(\varepsilon) = \frac{\dot{n}_{\text{in}}(\varepsilon)}{V_R} \tau(\varepsilon) \quad (100)$$

where $\dot{n}_{\text{in}}(\varepsilon)$ is the total number of electrons of energy ε accelerated per unit time, and $\tau(\varepsilon)$ is the electron lifetime. Let

$$\dot{n}_{\text{in}}(\varepsilon) = \dot{n}_{0,\text{in}} \left(\frac{\varepsilon}{\varepsilon_0} \right)^{-\kappa} \quad (101)$$

$$\tau(\varepsilon) = \tau_0 \left(\frac{\varepsilon}{\varepsilon_0} \right)^{\alpha} \quad (102)$$

With (100), the power law index of the electrons (97) is $\delta \approx \kappa - \alpha$.

Let a be the fraction of the energy that goes into accelerated particles, and b the fraction of the total coronal energy ultimately radiated into the observed X-ray band. Since some of the thermal energy is lost by conduction and other processes, $b < 1$. Then, X-rays are related to the total energy input

$$\dot{E} = \frac{1}{a} \int_{\varepsilon_0}^{\infty} \dot{n}_{\text{in}}(\varepsilon) \varepsilon d\varepsilon = \frac{1}{b} L_X. \quad (103)$$

Using (96)–(103), the relation between L_R and L_X becomes

$$L_R = 1.8 \cdot 4\pi \vartheta(B, \nu, \theta, \delta) \frac{a}{b} \varepsilon_0^{-1} \tau_0 \left(\frac{\alpha - 1}{\delta - 1} + 1 \right) L_X \quad (104)$$

where we require $\delta > 1$ and $\alpha > 2 - \delta$ for convergence. Equation (104) is general and includes different possible scenarios. Let us select typical parameters for stellar observations, viz. $\delta = 3$ (implying $\alpha > -1$), $\nu = 5$ GHz, and $\theta = 30^\circ$; then

$$L_R = 3.5 \cdot 10^{-22} B^{2.48} \frac{a}{b} \tau_0 (\alpha + 1) L_X \quad (105)$$

Late-type main-sequence and subgiant stars appear to follow a linear relation between L_R and L_X : $L_X \approx 10^{15.5} L_R$ (the coefficient is 0.5–1 dex smaller for RS CVn-type binaries; Güdel & Benz 1993, see Fig. 27). We thus suggest numerical relations between a , b , τ , and B for active stars:

$$B^{2.48} \frac{a}{b} \tau_0 (\alpha + 1) \approx \begin{cases} 9.0 \cdot 10^5 & \text{dMe, dKe, BY Dra} \\ 5.4 \cdot 10^6 & \text{RS CVn, Algols, PTTs, FK Com.} \end{cases} \quad (106)$$

Two scenarios are possible: If the acceleration efficiency a is close to unity, the nonthermal electrons first emit a small fraction of the total kinetic energy as synchrotron radiation before they lose most of their energy by collisions, thereby heating the X-ray emitting corona (“causal relation” between non-thermal and thermal energy). It is unknown whether fully efficient accelerators are realized in nature.

The other scenario implies a common energy release, most of it heating the corona by thermal processes (e.g. Ohmic heating), and a much smaller fraction a accelerating particles. Some of the latter energy may also end up as heat, but this is negligible. Therefore, the thermal plasma and nonthermal electrons radiate independently (“common origin” scenario). This scenario can explain the relation found by assuming that coronal heating in active stars *necessarily* implies electron acceleration to relativistic energies. The fraction between thermal and nonthermal energy release is the crucial, but unknown number. It is unclear whether it can be constant over many different types of stars.

The lifetime τ (or τ_0 and α) which is relevant here for the gyrosynchrotron emitting high-energy particles, depends on the process that scatters energetic electrons into the loss-cone of the trapped particle velocity distribution, such as collisions, whistler wave instability, or cyclotron maser action. Their effects on the relation between trapping time and particle energy are opposite. As an example, let us assume $\tau(\varepsilon) = \text{const}$ (i.e. $\alpha = 0$) and use solar active region and flare values for B (≈ 100 G) and a/b (order of unity; Dennis 1988; Withbroe & Noyes 1977). Equation (106) then would require $\tau \approx 10$ s for dM(e), dK(e), and BY Dra stars. The lifetime is an average over the time of flight of the particles that are lost immediately (moving parallel to the field lines) and the trapped particles temporarily residing in a lower density plasma. The estimated values for τ are compatible with the minimum observed time scale of variations in the “quiescent” emission (e.g. Jackson et al. 1989). For the halo of RS CVn binaries, B can be as low as ≈ 10 G (Mutel et al. 1985). Then, from (106), τ is of order of many hours, compatible with observed long time scales (e.g., Massi & Chiuderi-Drago 1992).

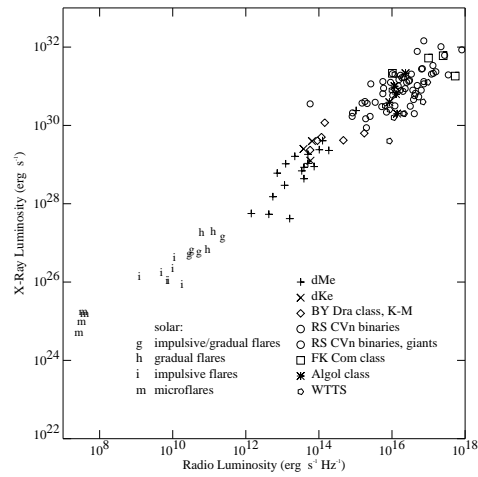


Fig. 27. Correlation between radio and X-ray luminosities for magnetically active stars (from Güdel 2002).

Acknowledgement. It is a pleasure to thank the organizers for inviting me to the Montegufoni summer school. I thank several colleagues for providing me figure material, which is reproduced with permission of the publishers. In particular, some of the material presented here has been reprinted, with permission, from the *Annual Review of Astronomy and Astrophysics*, Volume 40, © 2002 by Annual Reviews, www.annualreviews.org (Figures 1b, 2, 13–16, 22, 26, 27; Güdel 2002). Some material has been reprinted, with permission, from the *Astronomy and Astrophysics Review* Vol. 12 (Figures 1a, 4, 6–12, 18–25; Güdel 2004). Research at PSI has been supported by the Swiss National Science Foundation.

References

- M. Abada-Simon, A. Lecacheux, M. Aubier, J. A. Bookbinder: *A&A*, 321, 841 (1997)
M. Abada-Simon, A. Lecacheux, P. Louarn, G. A. Dulk, L. Belkora, et al.: *A&A*, 288, 219 (1994)
C. W. Ambruster, S. Sciortino, & L. Golub: *ApJS*, 65, 273 (1987)
P. André, T. Montmerle, E. D. Feigelson, P. C. Stine, K.-L. Klein: *ApJ*, 335, 940 (1988)
S. K. Antiochos: *ApJ*, 241, 385 (1980)
K. Arzner, M. Güdel: *ApJ*, 602, 363 (2004)
M. J. Aschwanden, R. W. Nightingale, D. Alexander: *ApJ*, 541, 1059 (2000)
M. Aschwanden, C. J. Schrijver: *ApJS*, 142, 269 (2002)
M. Audard, M. Güdel, J. J. Drake, V. Kashyap: *ApJ*, 541, 396 (2000)

- M. Audard, M. Güdel, E. F. Guinan: *ApJ*, 513, L53 (1999)
M. Audard, M. Güdel, S. L. Skinner: *ApJ*, 589, 983 (2003)
T. S. Bastian: *Sol. Phys.*, 130, 265 (1990)
T. S. Bastian, A. O. Benz, D. E. Gary: *ARA&A*, 36, 131 (1998)
T. S. Bastian, J. A. Bookbinder: *Nature*, 326, 678 (1987)
T. S. Bastian, J. Bookbinder, G. A. Dulk, M. Davis: *ApJ*, 353, 265 (1990)
A. J. Beasley, M. Güdel: *ApJ*, 529, 961 (2000)
A. O. Benz, W. Aref, M. Güdel: *A&A*, 298, 187 (1995)
A. O. Benz, J. Conway, M. Güdel: *A&A*, 331, 596 (1998)
R. J. Bray, L. E. Cram, C. J. Durrant, E. E. Loughhead: in *Plasma Loops in the Solar Corona* (Cambridge University Press, 1991)
P. J. Cargill: *ApJ*, 422, 381 (1994)
F. Chiuderi Drago, E. Franciosini: *ApJ*, 410, 301 (1993)
C. S. Choi, T. Dotani: *ApJ*, 492, 761 (1998)
E. W. Cliver, B. R. Dennis, A. L. Kiplinger, S. R. Kane, D. F. Neidig, N. R. Sheeley Jr., M. J. Koomen: *ApJ*, 305, 920 (1986)
A. Collura, L. Pasquini, J. H. M. M. Schmitt: *A&A*, 205, 197 (1988)
N. B. Crosby, M. J. Aschwanden, B. R. Dennis: *Solar Phys.*, 143, 275 (1993)
B. R. Dennis: *Sol. Phys.* 118, 49 (1988)
J. F. Dowdy Jr., R. L. Moore, S. T. Wu: *Solar Phys.*, 99, 79 (1985)
J. J. Drake, G. Peres, S. Orlando, J. M. Laming, A. Maggio: *ApJ*, 545, 1074 (2000)
S. A. Drake, D. C. Abbott, T. S. Bastian, J. H. Bieging, E. Churchwell, et al.: *ApJ*, 322, 902 (1987)
G. A. Dulk: *ARA&A*, 23, 169 (1985)
A. K. Dupree, N. S. Brickhouse, G. A. Doschek, J. C. Green, J. C. Raymond: *ApJ*, 418, L41 (1993)
U. Feldman, J. M. Laming, G. A. Doschek: *ApJ*, 451, L79 (1995)
A. H. Gabriel, C. Jordan: *MNRAS*, 145, 241 (1969)
D. E. Gary, J. L. Linsky: *ApJ*, 250, 284 (1981)
M. S. Giampapa, R. Rosner, V. Kashyap, T. A. Fleming, J. H. M. M. Schmitt, J. A. Bookbinder: *ApJ*, 463, 707 (1996)
M. Güdel: *ARA&A*, 40, 217 (2002)
M. Güdel: *A&AR*, 12, 71 (2004)
M. Güdel, K. Arzner, M. Audard, R. Mewe: *A&A*, 403, 155 (2003b)
M. Güdel, M. Audard, V. L. Kashyap, J. J. Drake, E. F. Guinan: *ApJ*, 582, 423 (2003a)
M. Güdel, M. Audard, H. Magee, E. Franciosini, N. Grosso, F. A. Cordova, R. Pallavicini, R. Mewe: *A&A*, 365, L344 (2001a)
M. Güdel, M. Audard, S. L. Skinner, M. I. Horvath: *ApJ*, 580, L73 (2002a)
M. Güdel, A. O. Benz: *A&A*, 211, L5 (1989)
M. Güdel, A. O. Benz: *A&A*, 231, 202 (1990)
M. Güdel, A. O. Benz: *ApJ*, 405, L63 (1993)

- M. Güdel, A. O. Benz, T. S. Bastian, E. Fürst, G. M. Simnett, R. J. Davis: *A&A*, 220, L5 (1989)
- M. Güdel, E. F. Guinan, S. L. Skinner: *ApJ*, 483, 947 (1997)
- M. Güdel, J. H. M. M. Schmitt: in *Röntgenstrahlung from the Universe*, eds. H. U. Zimmermann, J. E. Trümper, & H. Yorke (München: MPE, 1995), p. 35
- O. Havnes, C. K. Goertz: *A&A*, 138, 421 (1984)
- P. D. Jackson, M. R. Kundu, S. M. White: *ApJ*, 16, L85 (1987)
- P. D. Jackson, M. R. Kundu, S. M. White: *A&A*, 210, 284 (1989)
- J. Jakimiec, B. Sylwester, J. Sylwester, S. Serio, G. Peres, F. Reale: *A&A*, 253, 269 (1992)
- K. L. Jones, R. T. Stewart, G. J. Nelson: *MNRAS*, 274, 711 (1995)
- V. Kashyap, J. J. Drake, M. Güdel, M. Audard: *ApJ*, 580, 1118 (2002)
- K.-L. Klein, F. Chiuderi-Drago: *A&A*, 175, 179 (1987)
- R. A. Kopp, G. Poletto: *Sol. Phys.*, 93, 351 (1984)
- R. A. Kopp, G. Poletto: *ApJ*, 418, 496 (1993)
- M. R. Kundu, R. K. Shevgaonkar: *ApJ*, 297, 644 (1985)
- S. Krucker, A. O. Benz: *ApJ*, 501, L213 (1998)
- K. R. Lang, J. Bookbinder, L. Golub, M. M. Davis: *ApJ*, 272, L15 (1983)
- K. R. Lang, R. F. Willson: *ApJ*, 305, 363 (1986)
- K. R. Lang, R. F. Willson: *ApJ*, 326, 300 (1988)
- R. P. Lin, R. A. Schwartz, S. R. Kane, R. M. Pelling, K. Hurley: *ApJ*, 283, 421 (1984)
- J. L., Linsky, S. A. Drake, T. S. Bastian: *ApJ*, 393, 341 (1992)
- J. L. Linsky, D. E. Gary: *ApJ*, 274, 776 (1983)
- J. L. Linsky, B. M. Haisch: *ApJ*, 229, L27 (1979)
- J. L. Linsky, B. E. Wood, A. Brown, R. Osten: *ApJ*, 492, 767 (1998)
- L. B. Lucy: *AJ*, 79, 745 (1974)
- A. Maggio, G. Peres: *A&A*, 325, 237 (1997)
- A. Marino, G. Micela, G. Peres: *A&A*, 353, 177 (2000)
- M. Massi, F. Chiuderi-Drago: *A&A*, 253, 403 (1992)
- Melrose, D. B.: *Plasma Astrophysics* (Gordon and Breach, New York, 1980)
- R. Mewe, E. H. B. M. Gronenschild, G. H. J. van den Oord: *A&AS*, 62, 197 (1985)
- R. Mewe, J. S. Kaastra, G. H. J. van den Oord, J. Vink, Y. Tawara: *A&A*, 320, 147 (1997)
- D. H. Morris, R. L. Mutel, B. Su: *ApJ*, 362, 299 (1990)
- R. L. Mutel, J.-F. Lestrade, R. A. Preston, R. B. Phillips: *ApJ*, 289, 262 (1985)
- R. L. Mutel, L. A. Molnar, E. B. Waltman, F. D. Ghigo: *ApJ*, 507, 371 (1998)
- R. L. Mutel, D. H. Morris, D. J. Doiron, J.-F. Lestrade: *AJ*, 93, 1220 (1987)
- J.-U. Ness, M. Güdel, J. H. M. M. Schmitt, M. Audard, A. Telleschi: *A&A*, 427, 667 (2004)
- R. A. Osten, T. S. Bastian: *ApJ*, 637, 1016 (2006)

- R. A. Osten, T. R. Ayres, A. Brown, J. L. Linsky, A. Krishnamurthi: *ApJ*, 582, 1073 (2003)
- R. A. Osten, A. Brown: *ApJ*, 515, 746 (1999)
- R. Pallavicini, G. Tagliaferri, L. Stella: *A&A*, 228, 403 (1990)
- H. C. Pan, C. Jordan, K. Makishima, R. A. Stern, K. Hayashida, M. Inda-Koide: *MNRAS*, 285, 735 (1997)
- E. N. Parker: *ApJ*, 330, 474 (1988)
- C. E. Parnell, P. E. Jupp: *ApJ*, 529, 554 (2000)
- V. Petrosian: *ApJ*, 299, 987 (1985)
- K. J. H. Phillips, M. Mathioudakis, D. P. Huenemoerder, D. R. Williams, M. E. Phillips, F. P. Keenan: *MNRAS*, 325, 1500 (2001)
- G. Poletto, R. Pallavicini, R. A. Kopp: *A&A*, 201, 93 (1988)
- D. Porquet, R. Mewe, J. Dubau, A. J. J. Raassen, J. S. Kaastra: *A&A*, 376, 1113 (2001)
- P. Preś, M. Siarkowski, J. Sylwester: *MNRAS*, 275, 43 (1995)
- F. Reale, R. Betta, G. Peres, S. Serio, J. McTiernan: *A&A*, 325, 782 (1997)
- F. Reale, S. Serio, G. Peres: *A&A*, 272, 486 (1993)
- R. Rosner, W. H. Tucker, G. S. Vaiana: *ApJ*, 220, 643 (1978)
- J. H. M. M. Schmitt, F. Favata: *Nature*, 401, 44 (1999)
- J. H. M. M. Schmitt, J.-U. Ness, G. Franco: *A&A*, 412, 849 (2003)
- C. J. Schrijver, M. J. Aschwanden: *ApJ*, 566, 1147 (2002)
- C. J. Schrijver, J. R. Lemen, R. Mewe: *ApJ*, 341, 484 (1989)
- C. J. Schrijver, R. Mewe, G. H. J. van den Oord, J. S. Kaastra: *A&A*, 302, 438 (1995)
- S. Serio, G. Peres, G. S. Vaiana, L. Golub, R. Rosner: *ApJ*, 243, 288 (1981)
- S. Serio, F. Reale, J. akimiec, B. Sylwester, J. Sylwester: *A&A*, 241, 197 (1991)
- K. Shibata, T. Yokoyama: *ApJ*, 526, L49 (1999)
- K. Shibata, T. Yokoyama: *ApJ*, 577, 422 (2002)
- M. Siarkowski, P. Preś, S. A. Drake, N. E. White, K. P. Singh: *ApJ*, 473, 470 (1996)
- L. Spitzer: *Physics of Fully Ionized Gases*, (New York: Interscience, 1962)
- R. A. Stern, S. K. Antiochos, F. R. Harnden Jr.: *ApJ*, 305, 417 (1986)
- A. Telleschi, M. Güdel, K. R. Briggs, M. Audard, J.-U. Ness, S. L. Skinner: *ApJ*, 622, 653 (2005)
- C. Triglio C. S. Buemi, G. Umana, M. Rodonò, P. Leto, et al.: *A&A*, 373, 181 (2001)
- G. Umana, P. Leto, C. Triglio, R. M. Hjellming, S. Catalano: *A&A*, 342, 709 (1999)
- G. Umana, C. Triglio, S. Catalano: *A&A*, 329, 1010 (1998)
- G. Umana, C. Triglio, R. M. Hjellming, S. Catalano, M. Rodonò: *A&A*, 267, 126 (1993)
- G. H. J. van den Oord, R. Mewe: *A&A*, 213, 245 (1989)
- G. H. J. van den Oord, R. Mewe, A. C. Brinkman: *A&A*, 205, 181 (1988)

- G. H. J. van den Oord, C. J. Schrijver, M. Camphens, R. Mewe, J. S. Kaastra: A&A, 326, 1090 (1997)
- R. Ventura, A. Maggio, G. Peres: A&A, 334, 188 (1998)
- J. F. Vesecky, S. K. Antiochos, J. H. Underwood: ApJ, 233, 987 (1979)
- F. M. Walter, D. M. Gibson, G. Basri: ApJ, 267, 665 (1983)
- N. E. White, J. L. Culhane, A. N. Parmar, B. J. Kellett, S. Kahn, G. H. J. van den Oord, J. Kuijpers: ApJ, 301, 262 (1986)
- N. E. White, R. A. Shafer, K. Horne, A. N. Parmar, J. L. Culhane: ApJ, 350, 776 (1990)
- S. M. White, E. Franciosini: ApJ, 444, 342 (1995)
- S. M. White, M. R. Kundu, P. D. Jackson: A&A, 225, 112 (1989)
- S. M. White, J. Lim, M. R. Kundu: ApJ, 422, 293 (1994)
- G. L. Withbroe: Solar Phys., 45, 301 (1975)
- G. L. Withbroe, R. W. Noyes: ARA&A, 15, 363 (1977)